Supplement of Atmos. Chem. Phys., 23, 7177–7212, 2023
https://doi.org/10.5194/acp-23-7177-2023-supplement

Atmospheric Chemistry and Physics
Open Access

Supplement of

Insights into the size-resolved dust emission from field measurements in the Moroccan Sahara

Cristina González-Flórez et al.

Correspondence to: Cristina González-Flórez (cristina.gonzalez@bsc.es)

Contents

S1 Surface particle size distributions at the L'Bour measurement site

The surface of our measurement site at L'Bour consists mainly of a paved sediment surrounded by small sand dunes. Fig. S1 shows the PSDs of samples taken for both surface types analyzed in dry (minimally dispersed) and wet dispersion (fully dispersed) along with pictures of the corresponding surfaces. Details on the sampling and analysis methods are provided in González-Romero et al. (2023).

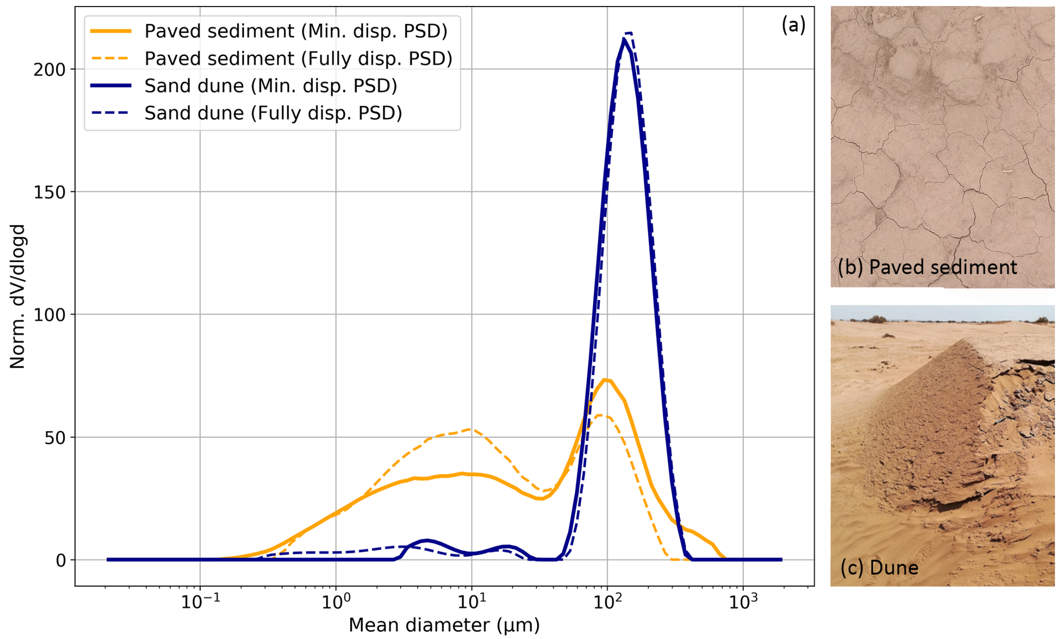

Figure S1. (a) Minimally and fully dispersed normalized mean PSDs of a sand dune (blue) and the paved sediments (orange) in L'Bour. (b) Picture of the paved sediment. (c) Picture of a small sand dune in L'Bour.

S2 Comparison between optical and geometric diameters

Fig. S2 displays in both linear and logarithmic scales the default optical diameters of the Fidas OPC versus the associated geometric diameters whose calculation is described in Sect. 2.2.2 in the main paper and some specifications are given in Appendix A.

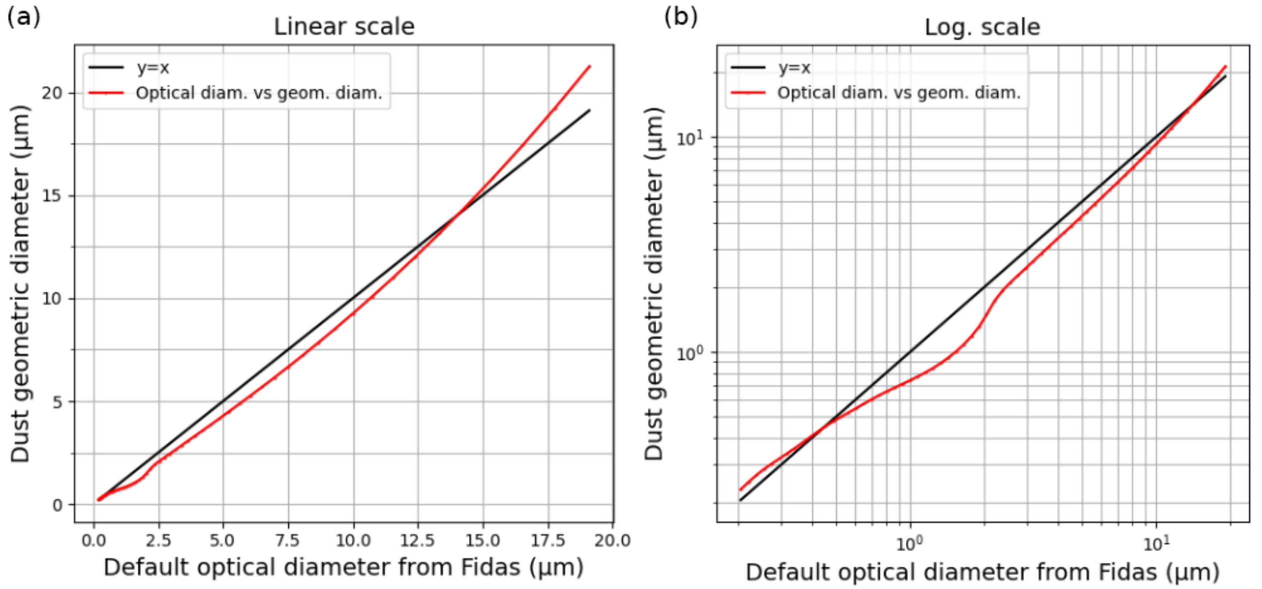

Figure S2. Default optical diameters (µm) of the Fidas versus geometric diameters (µm) calculated assuming that dust particles are tri-axial ellipsoids with an aspect ratio (AR) of 1.46, a height-to-width ratio (HWR) of 0.45 and a refractive index of 1.49 + 0.0015 i. (a) Representation in linear scale. (b) Representation in logarithmic scale.

S3 Threshold friction velocity

The threshold friction velocity u_{*th} is calculated fitting the saltation flux Q versus the wind shear stress τ. Following Martin and Kok (2017), we consider both the classical models where fluid lifting plays a role in particle entrainment, leading to nonlinear 3/2 stress-flux scaling (i.e., $Q \sim \tau^{3/2}$ or alternatively $Q \sim u_*^3$) and the more recent models in which splash-dominated entrainment leads to linear or nearly linear stress-flux scaling (i.e., $Q \sim \tau$ or alternatively $Q \sim u_*^2$). Our measurements shown in Fig. S3 seem to slightly better fit the 3/2 form $Q = Cu_*(\tau - \tau_{th})$ (magenta line) than the linear fit $Q = C(\tau - \tau_{th})$ (green line), where C and the impact threshold stress τ_{th} are the fitting parameters reported in the graph along with the standard error of the estimate for each regression model. Therefore, in this study we consider $u_{*th} = (\tau_{th}/\overline{\rho_{air}})^{1/2} = 0.16\,\mathrm{m\,s^{-1}}$, where $\overline{\rho_{air}} = 1.07\,\mathrm{kg\,m^{-3}}$ is the mean air density taking into account the periods when there is a simultaneous net positive diffusive flux and saltation flux, the diffusive flux is positive in all size bins above 0.4 µm and $u_* > 0.1\,\mathrm{m\,s^{-1}}$.

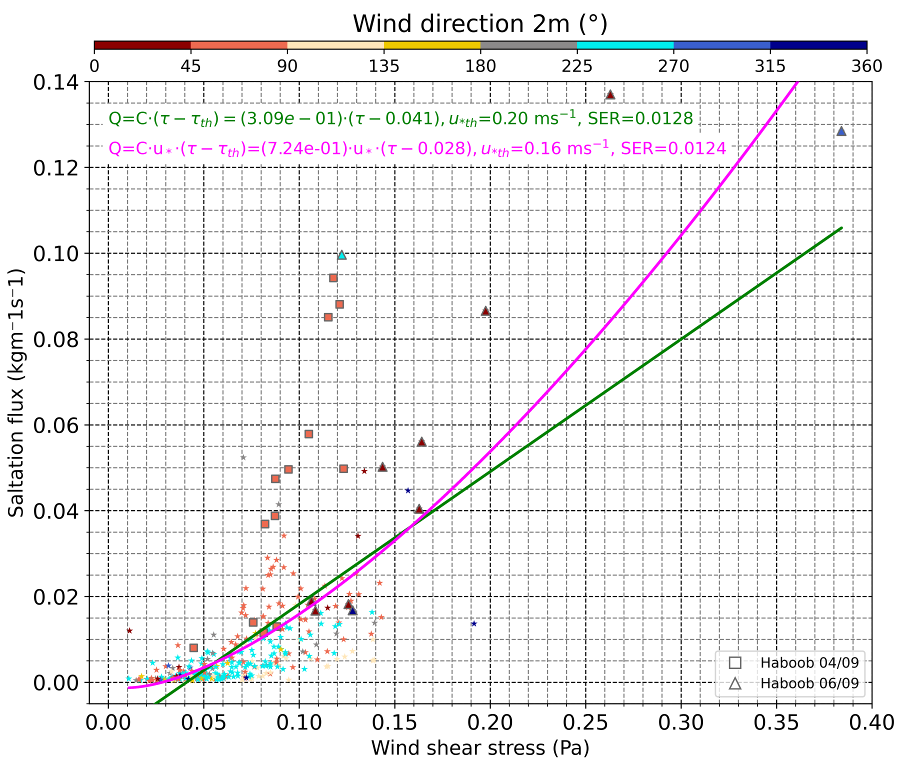

Figure S3. Saltation flux ($\mathrm{kg\,m^{-1}\,s^{-1}}$) versus wind shear stress (Pa). The points correspond to the 15-min values in which 1) there is a simultaneous net positive diffusive flux and saltation flux, 2) the diffusive flux is positive in all size bins above 0.4 µm and 3) $u_* > 0.1\,\mathrm{m\,s^{-1}}$. Squares and triangles are used to identify the values corresponding to haboobs on 4th and 6th September, respectively. The green and magenta lines represent respectively the regression curves of the form $Q = C\cdot(\tau - \tau_{th})$ and $Q = C\cdot u_*\cdot(\tau - \tau_{th})$. The fitting parameters C and τ_{th} for these respective linear and 3/2 fits are shown in the graph along with the standard error of the estimate for each case.

S4 Wind rose at L'Bour measurement site

Winds were generally channelled through the valley, broadly parallel to the Drâa river bed (Fig. 1c), alternating between two opposite and preferential wind directions, centered around 80 ° and 240 ° as shown in Fig. S4, where colours represent different u_* intervals.

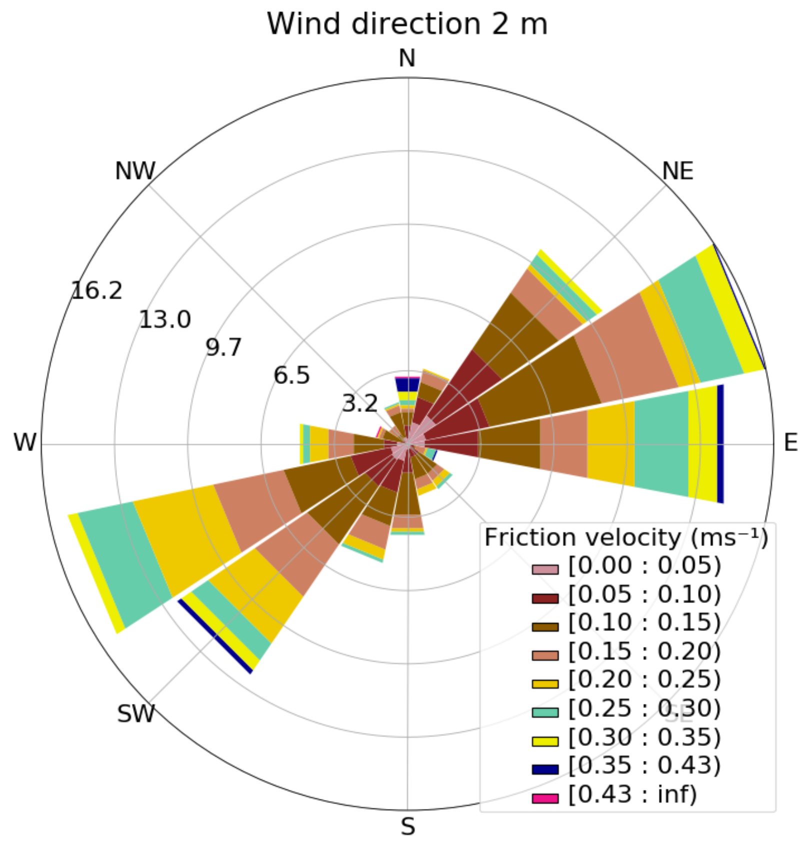

Figure S4. Wind rose at 2 m height for different u_* intervals ($\mathrm{m\,s^{-1}}$). The length of each bar represents the fraction of time the wind blows from that direction.

S5 Time series of dust concentrations and size-resolved mass fractions

The presence of particles with diameters below ∼0.4 µm that have an anthropogenic origin, as explained in Sect. 3.3.1 in the main paper, is better appreciated in Fig. S5, where size-resolved concentrations from FidasL (colour contours in right y-axis) are represented as number and mass fractions (%).

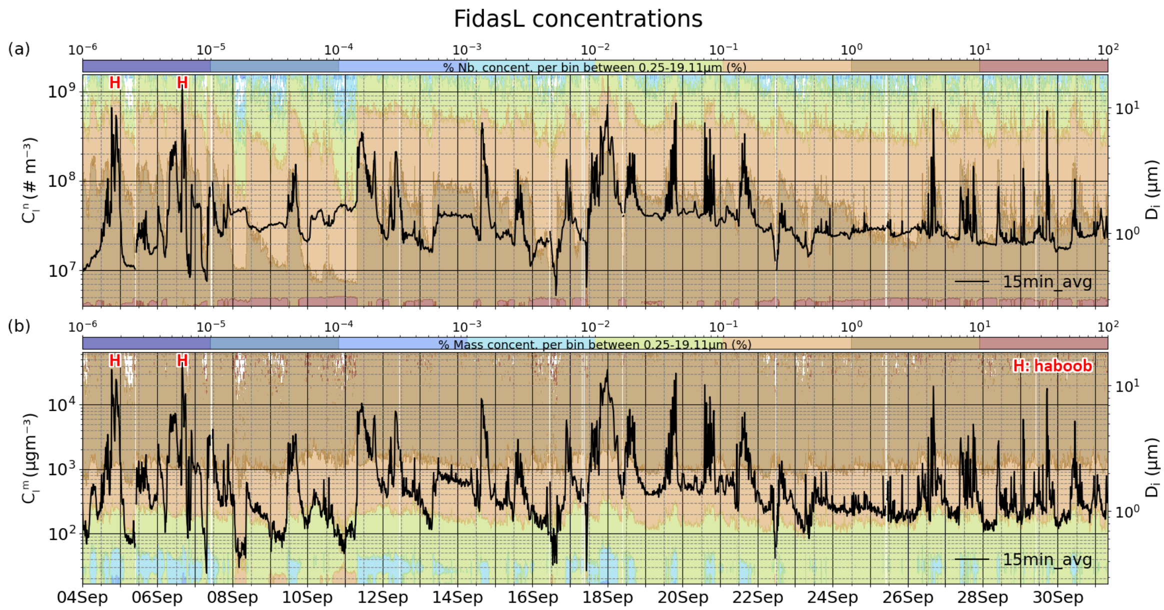

Figure S5. Solid lines represent the time evolution of the 15-min average total particle concentrations between 0.25 to 19.11 µm in number (# m^{-3}) (a) and mass ($\mu g m^{-3}$) (b). Contour plots on the background show the size-resolved particle number (a) and mass (b) concentration fractions (%) for each time step.

S6 Additional information on saltation and sandblasting efficiency at L'Bour

Figs. S6 and S7 are similar to Fig. 5 but are done selecting only the 15-min values corresponding to the two predominant wind directions (45–90 ° and 225–270 °).

Tables S1, S2 and S3 report the parameters a and b derived from each regression curve in Figs. 5, S6 and S7, respectively, and their 95% confidence intervals.

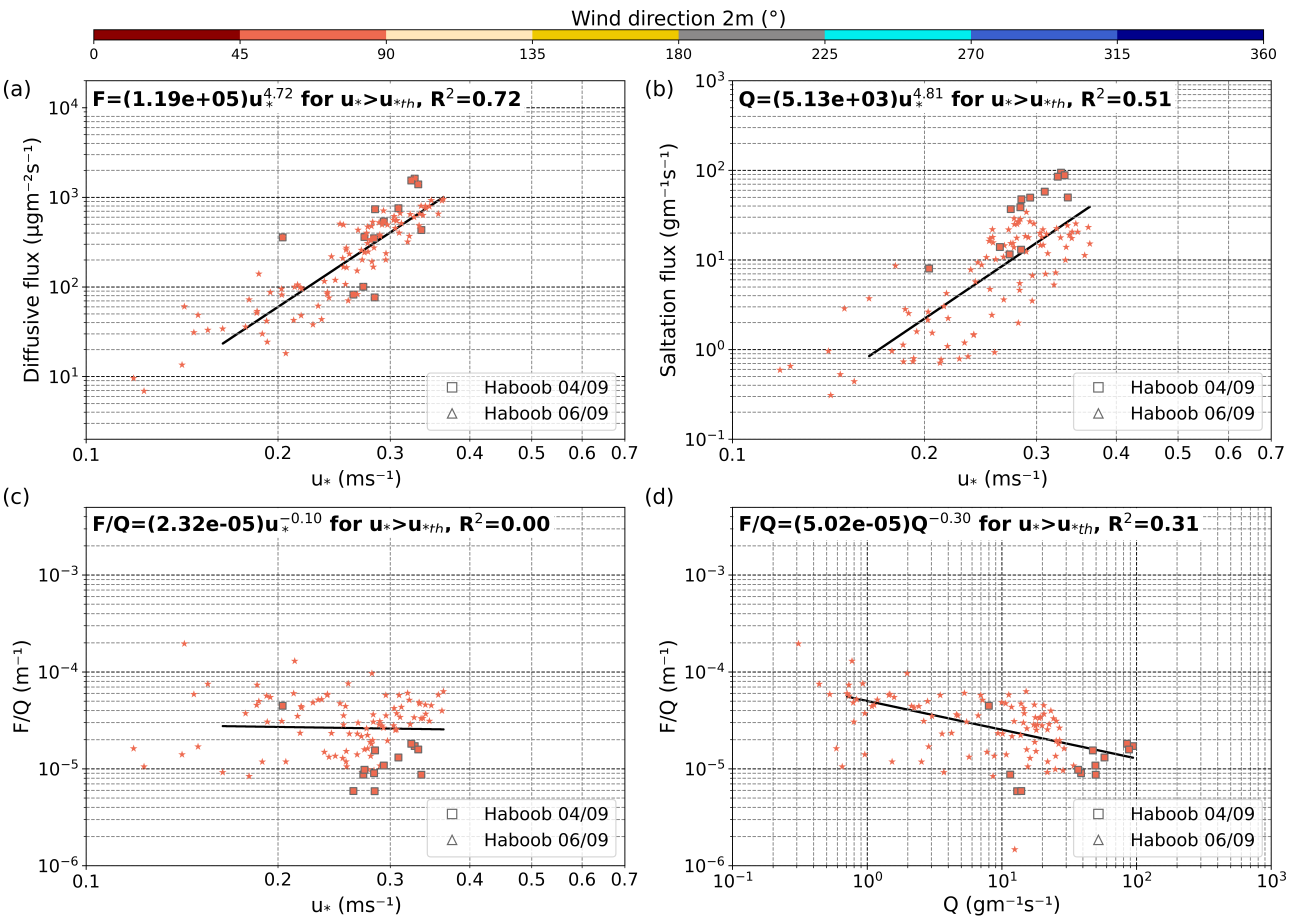

Figure S6. (a) Diffusive flux ($\mu g\,m^{-2}\,s^{-1}$) versus friction velocity u_* ($m\,s^{-1}$); (b) Saltation flux ($g\,m^{-1}\,s^{-1}$) versus u_* ($m\,s^{-1}$); (c) Sandblasting efficiency (m^{-1}) versus u_* ($m\,s^{-1}$); (d) Sandblasting efficiency (m^{-1}) versus saltation flux ($g\,m^{-1}\,s^{-1}$). The points shown in all panels correspond to the 15-min values in which 1) there is a simultaneous net positive diffusive flux and saltation flux, 2) the diffusive flux is positive in all size bins with D_i > 0.4 μm and 3) wind direction is between 45–90 °. We consider the bulk diffusive flux between 0.37 and 19.11 μm. Squares and triangles are used to identify the values corresponding to haboobs on 4th and 6th September, respectively. The lines in (a)-(d) represent the regression curves of the form $a \cdot u_*^b$ for $u_* > u_{*th}$. The coefficient of determination (in logarithmic space) of each regression curve is shown in its respective graph and the parameters a and b along with their respective 95% confidence intervals are reported in Table S2.

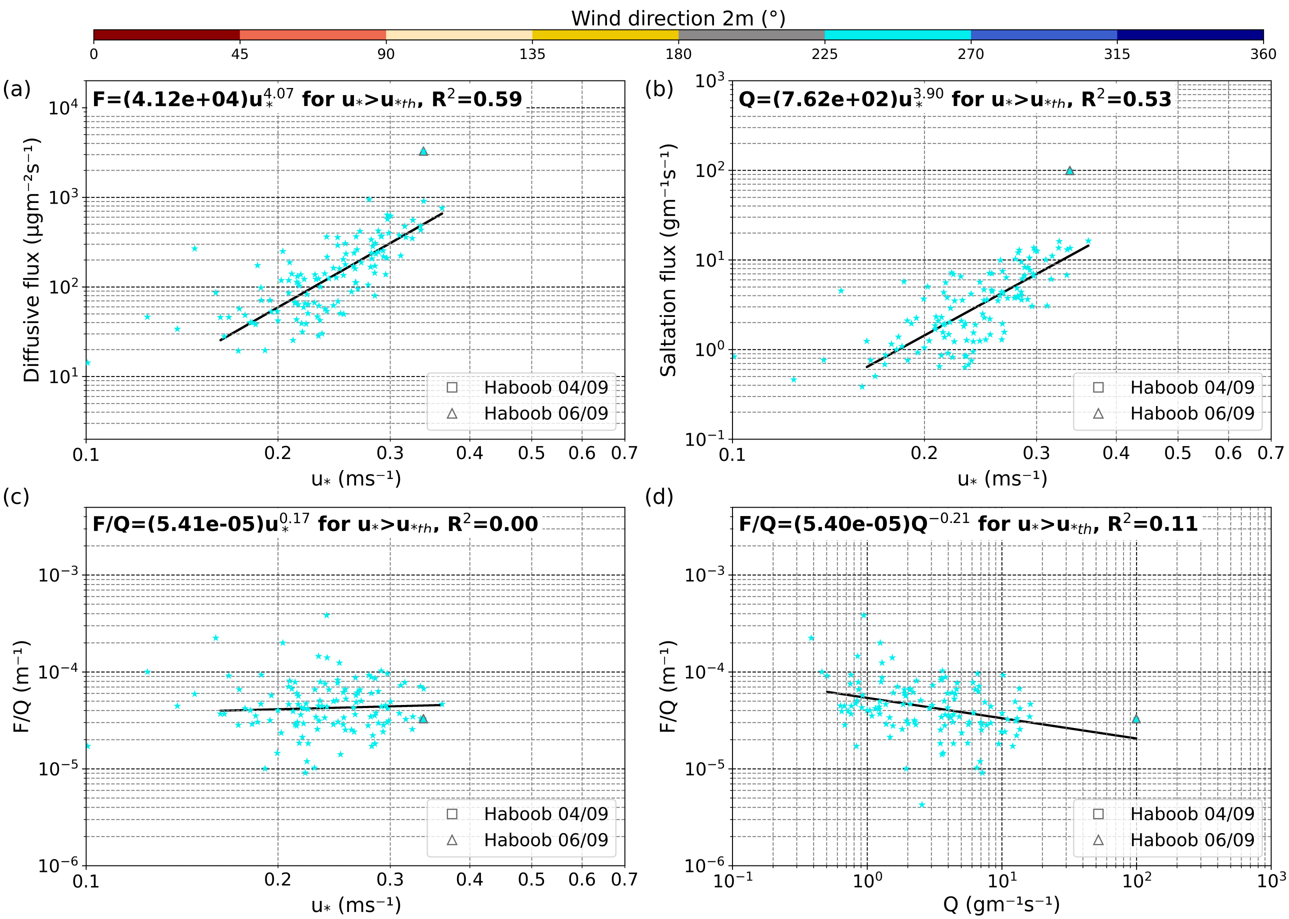

Figure S7. (a) Diffusive flux ($\mu g\,m^{-2}\,s^{-1}$) versus friction velocity u_* ($m\,s^{-1}$); (b) Saltation flux ($g\,m^{-1}\,s^{-1}$) versus u_* ($m\,s^{-1}$); (c) Sandblasting efficiency (m^{-1}) versus u_* ($m\,s^{-1}$); (d) Sandblasting efficiency (m^{-1}) versus saltation flux ($g\,m^{-1}\,s^{-1}$). The points shown in all panels correspond to the 15-min values in which 1) there is a simultaneous net positive diffusive flux and saltation flux, 2) the diffusive flux is positive in all size bins with $D_i > 0.4\,\mu m$ and 3) wind direction is between 225–270 °. We consider the bulk diffusive flux between 0.37 and 19.11 µm. Squares and triangles are used to identify the values corresponding to haboobs on 4th and 6th September, respectively. The lines in (a)-(d) represent the regression curves of the form $a \cdot u_*^b$ for $u_* > u_{*th}$. The coefficient of determination (in logarithmic space) of each regression curve is shown in its respective graph and the parameters a and b along with their respective 95% confidence intervals are reported in Table S3.

Table S1. Obtained parameters a and b from each regression curve in Fig. 5 along with their 95% confidence intervals.

a	a [95% C.I.]	b	b [95% C.I.]
	$F = a \cdot u_*^b$		
$3.45 \cdot 10^4$	$[2.15, 5.53] \cdot 10^4$	3.88	[3.54, 4.23]
	$Q = a \cdot u_*^b$		
$16.74 \cdot 10^2$	$[8.84, 31.68] \cdot 10^2$	4.31	[3.85, 4.78]
	$F/Q = a \cdot u_*^b$		
$2.06 \cdot 10^{-5}$	$[1.19, 3.55] \cdot 10^{-5}$	−0.43	[−0.83, −0.04]
	$F/Q = a \cdot Q^b$		
$6.24 \cdot 10^{-5}$	$[5.58, 6.98] \cdot 10^{-5}$	−0.33	[−0.39, −0.28]

Table S2. Obtained parameters a and b from each regression curve in Fig. S6 (wind directions between 45–90 °) along with their 95% confidence intervals.

a	a [95% C.I.]	b	b [95% C.I.]
	$F = a \cdot u_*^b$		
$11.92 \cdot 10^4$	$[5.39, 26.36] \cdot 10^4$	4.72	[4.13, 5.31]
	$Q = a \cdot u_*^b$		
$51.32 \cdot 10^2$	$[14.66, 179.80] \cdot 10^2$	4.81	[3.88, 5.75]
	$F/Q = a \cdot u_*^b$		
$2.32 \cdot 10^{-5}$	$[0.89, 6.04] \cdot 10^{-5}$	−0.10	[−0.81, 0.62]
	$F/Q = a \cdot Q^b$		
$5.02 \cdot 10^{-5}$	$[4.02, 6.26] \cdot 10^{-5}$	−0.30	[−0.39, −0.21]

Table S3. Obtained parameters a and b from each regression curve in Fig. S7 (wind directions between 225–270 °) along with their 95% confidence intervals.

a	a [95% C.I.]	b	b [95% C.I.]
	$F = a \cdot u_*^b$		
$4.12 \cdot 10^4$	$[1.69, 10.06] \cdot 10^4$	4.07	[3.44, 4.69]
	$Q = a \cdot u_*^b$		
$7.62 \cdot 10^2$	$[2.90, 19.98] \cdot 10^2$	3.90	[3.22, 4.57]
	$F/Q = a \cdot u_*^b$		
$5.41 \cdot 10^{-5}$	$[2.23, 13.10] \cdot 10^{-5}$	0.17	[−0.45, 0.79]
	$F/Q = a \cdot Q^b$		
$5.40 \cdot 10^{-5}$	$[4.59, 6.35] \cdot 10^{-5}$	−0.21	[−0.32, −0.10]

S7 Relationship between roughness length and friction velocity

Figure S8 displays the roughness length z_0 against u_* under saltation conditions, that is 15-min values with a positive saltation flux, in our site. We only use the values in which at the same time $u_* > u_{*th}$. z_0 shows quite a lot of scatter, particularly for u_* below $0.2\,\mathrm{m\,s^{-1}}$. We also observe that z_0 is sensitive to wind direction. For example z_0 can reach about one order of magnitude higher values for wind directions 135–180 ° and 315–360 °, the latter one close to the alignment of our instruments. There are also differences, albeit relatively small, between the two predominant wind directions, 225–270 ° and 45–90 °.

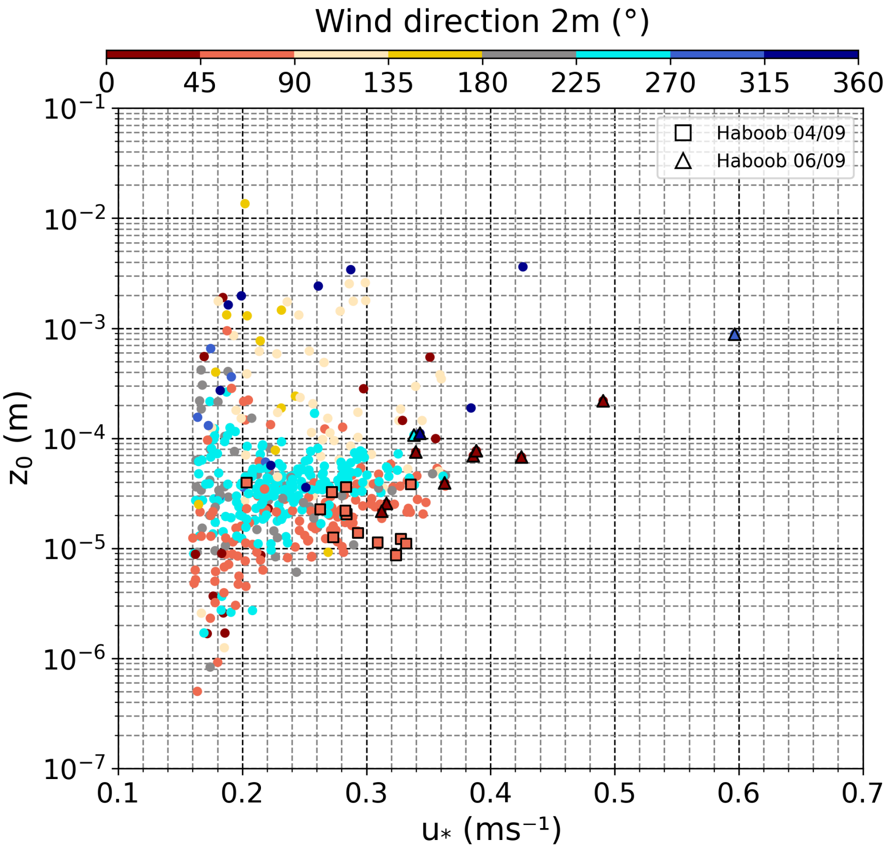

Figure S8. Relationship between 15-min averages of surface roughness length (z_0) and friction velocity (u_*) under wind erosion conditions. Colors indicate wind direction at 2 m height. Squares and triangles are used to identify the values corresponding to haboobs on 4th and 6th September, respectively.

In Fig. S9a our measurements are fitted to the relationship $z_0 = C_c \cdot u_*^2/g$ originally derived by Charnock (1955) for water surfaces, but that can be applied for sand and snow surfaces (Owen, 1964; Chamberlain, 1983). We obtain $C_c = 0.02$ when taking into account all data, although the dispersion is very high and R^2 (in logarithmic space) very low. This value coincides with that obtained by Owen (1964) and that derived in Dupont et al. (2018) for some of the wind erosion events during the WIND-O-V 2017 Experiment. Smaller values of $C_c = 0.007$ and 0.004 and a higher R^2 (in logarithmic space) are obtained, when considering separately the predominant wind directions 225–270 ° and 45–90 °, respectively (Fig. S9a). Our measurements are fitted as well to the modified Charnock's model proposed by Sherman (1992), which uses a more physical relation and accounts for the presence of a threshold $z_0 - (2D_{50}/30) = C_c \cdot (u_* - u_{*th})^2/g$, where $2D_{50}/30$ represents the minimum plausible roughness length, being D_{50} the mean grain diameter, and $u_* - u_{*th}$ the excess shear velocity. We have considered

D_{50} to be the volume median diameter of the saltators at our site, that is $0.13\,\mathrm{mm}$ and $u_{*th} = 0.16\,\mathrm{m\,s^{-1}}$, as described in Section S3. In this case we obtain $C_c = 0.07$ when taking into account all data and $C_c = 0.02$ and 0.01, when considering separately the predominant wind directions 225–$270\,^\circ$ and 45–$90\,^\circ$, respectively (Fig. S9b). A lower R^2 (in logarithmic space) is obtained in the three cases compared to Charnock's model. In Fig. S9 we use 15-min data with a positive saltation flux and when $u_* > u_{*th}$ while in Fig. S10 we only select the values when $u_* > 0.2\,\mathrm{m\,s^{-1}}$. In the latter, C_c values remain without many changes but we observe a significant increase in R^2 (in logarithmic space).

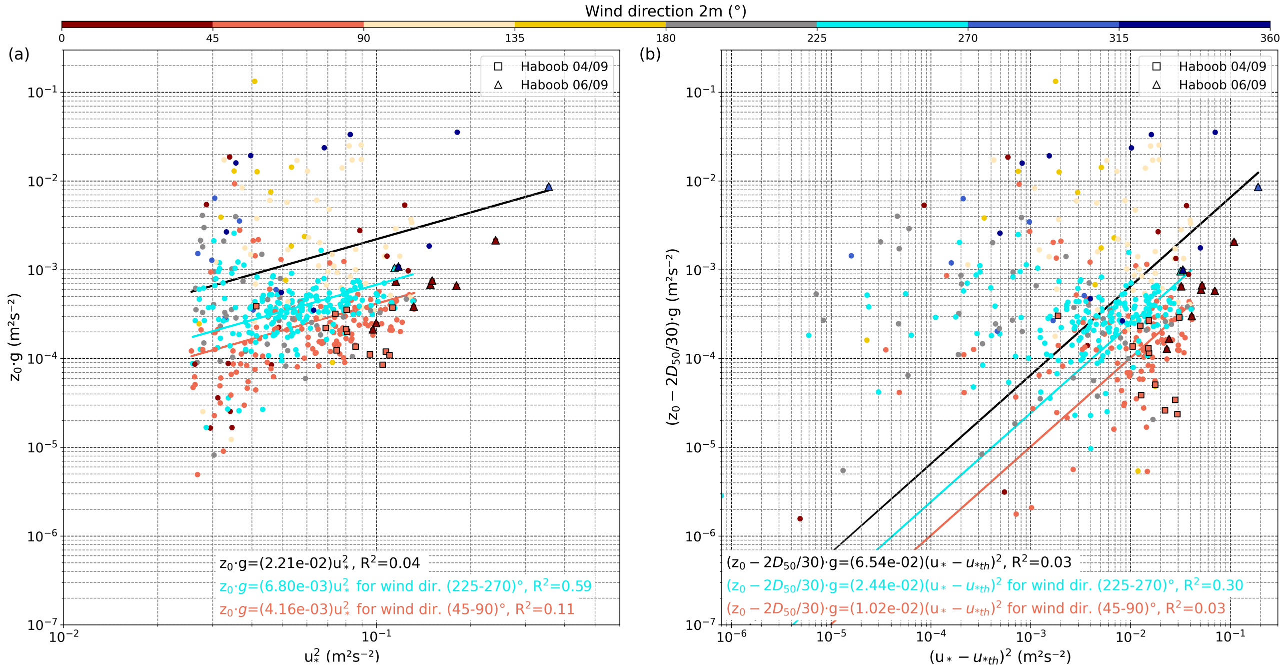

Figure S9. Relationship between 15-min averages of surface roughness length (z_0) and friction velocity (u_*) under wind erosion conditions. Colors indicate wind direction at $2\,\mathrm{m}$ height. The lines represent the regression curves of the form $C_c \cdot u_*^2/g$ for all the data (grey) and for wind directions between 45–$90\,^\circ$ (orange) and 225–$270\,^\circ$ (blue). The resulting fit-parameters and coefficients of determination are given in the figure. Squares and triangles are used to identify the values corresponding to haboobs on 4th and 6th September, respectively.

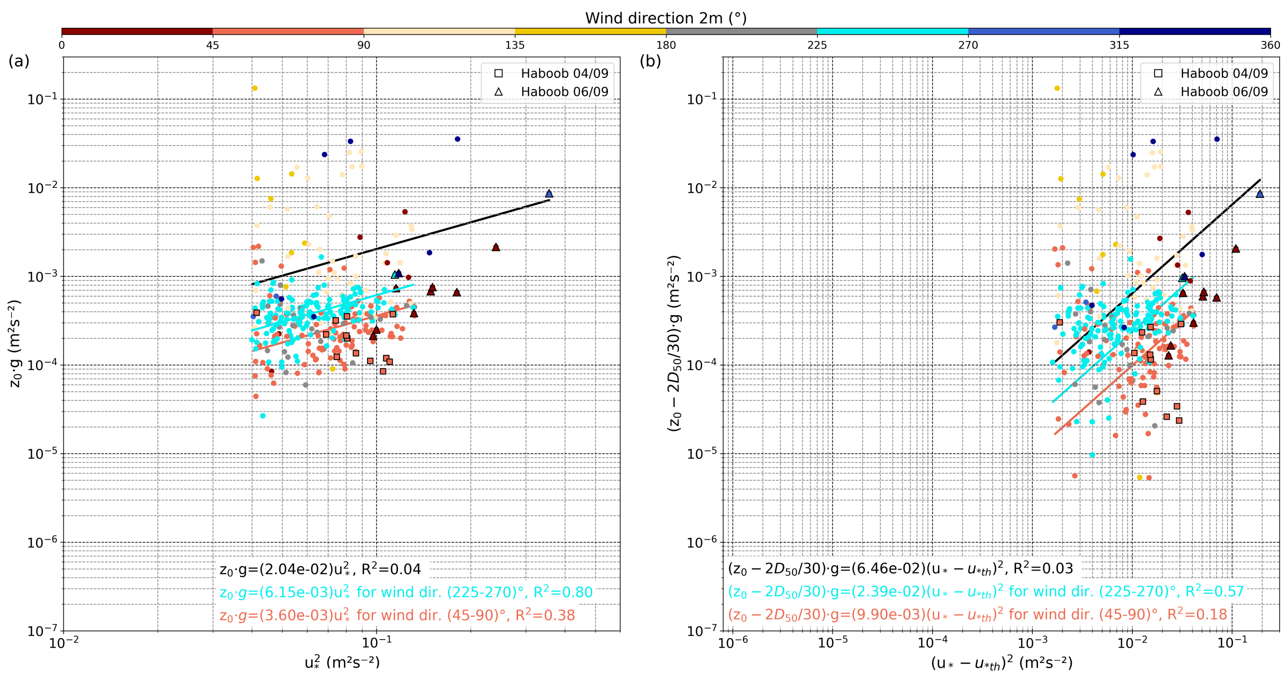

Figure S10. Relationship between 15-min averages of surface roughness length (z_0) and friction velocity (u_*) under wind erosion conditions. Colors indicate wind direction at 2 m height. The lines represent the regression curves of the form $C_c \cdot u_*^2/g$ for all the data (grey) and for wind directions between 45–90° (orange) and 225–270° (blue). The resulting fit-parameters and coefficients of determination are given in the figure. Squares and triangles are used to identify the values corresponding to haboobs on 4th and 6th September, respectively.

S8 PSDs obtained with FidasU

Figs. S11 and S12 are equivalent to Figs. 6 and 7, but using data from FidasU after correcting the systematic deviation (see Appendix B). As it is usual, as the height increases dust concentration decreases. However, we find the same features (explained in Sect. 3.3) than for FidasL.

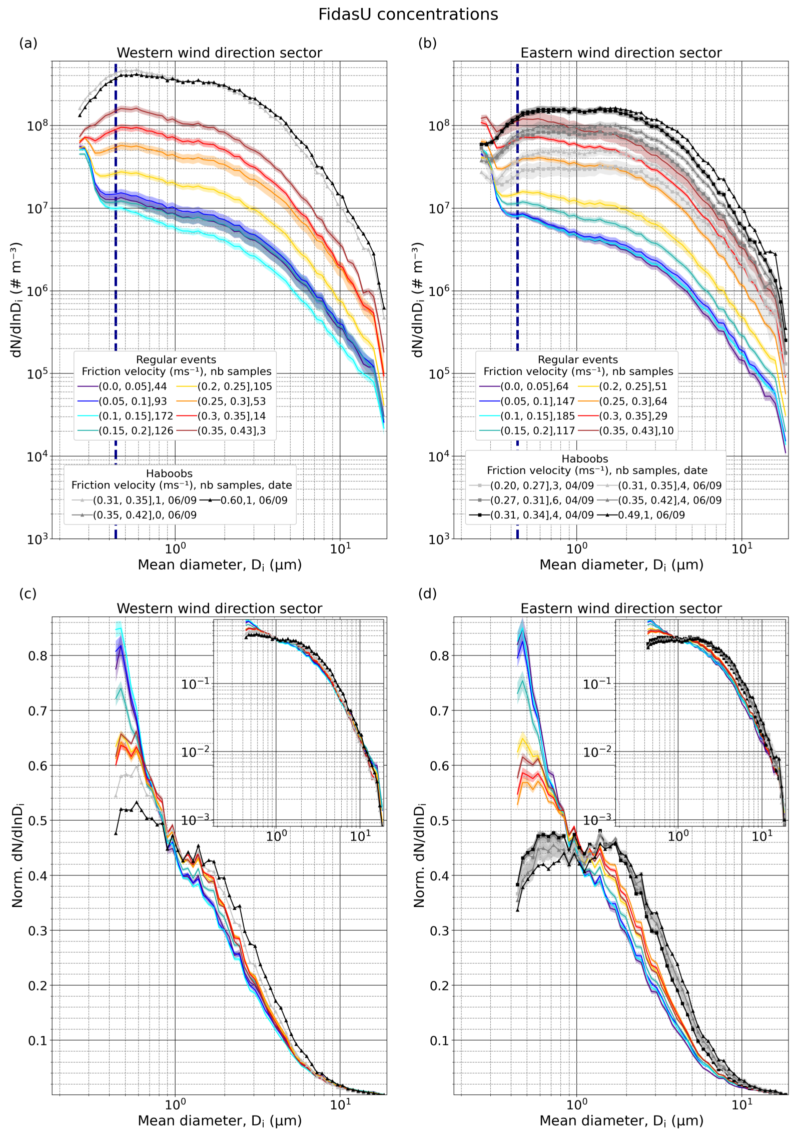

Figure S11. Average size-resolved particle number concentration, $dN/dlnD_i$ ($\# \, \mathrm{m}^{-3}$), for different u_* intervals, types of events (regular or haboob), and wind directions in the range 150–330 $^\circ$ (a) and 330–150 $^\circ$ (b). The number of available 15-min average PSDs in each u_* interval is indicated in the legend. Panels (c)-(d) are the same as (a)-(b) but normalized ($Norm.\ dN/dlnD_i$) after removing the anthropogenic mode (normalization from 0.42 to 19.11 µm). The insets show the same data but with logarithmic ordinate axis scaling. Shaded areas around the lines depict the standard error. The shown PSDs were obtained from FidasU. In (a) and (b) the dashed dark blue line marks the end of the anthropogenic mode ($D_i = 0.44\,\mathrm{\mu m}$). Data are shown using original size bin resolution, but first 3 bins are not represented as Fidas is considered efficient from the fourth one onward.

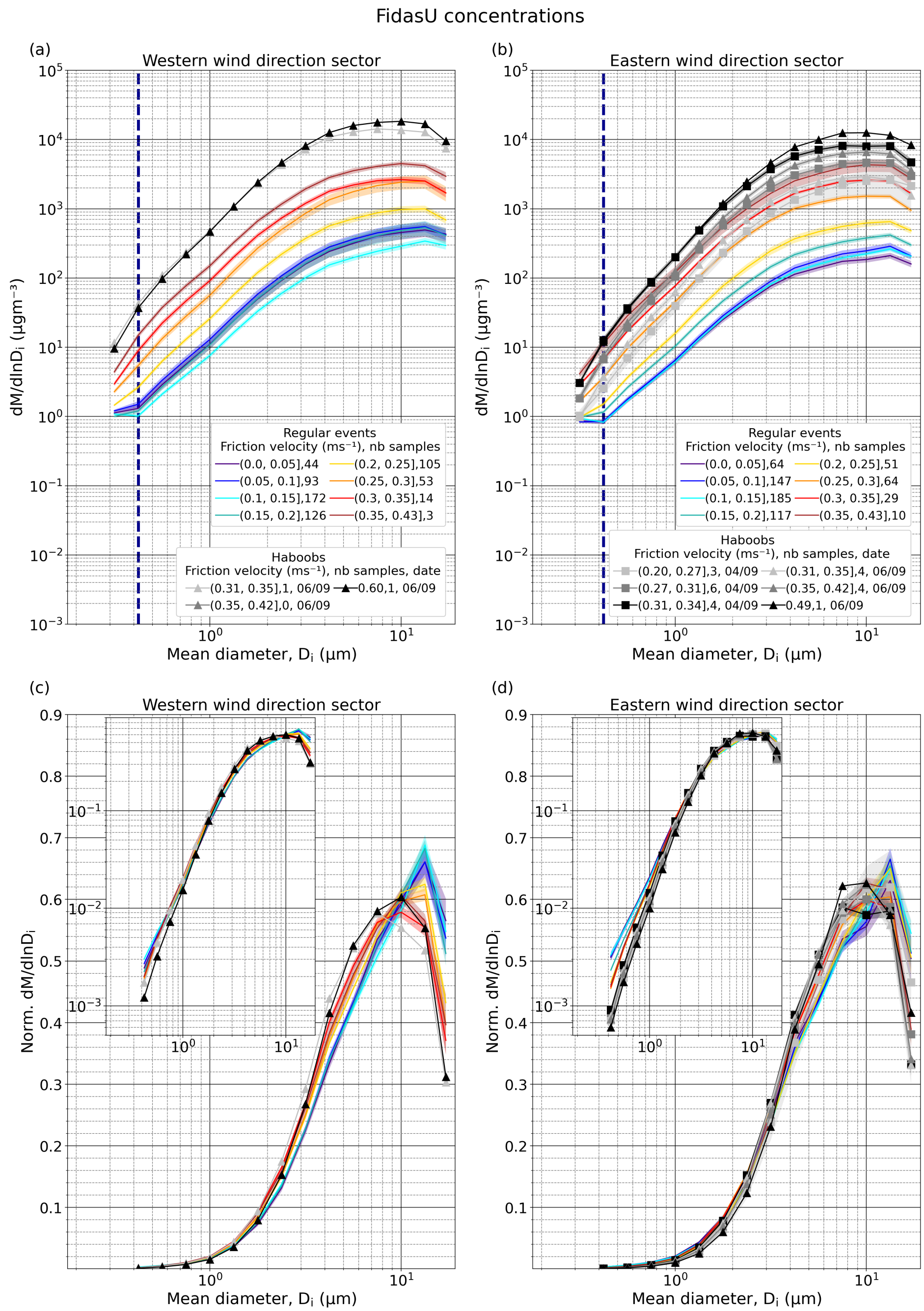

Figure S12. Average size-resolved particle mass concentration, $dM/dlnD_i$ ($\mu g\, m^{-3}$), for different u_* intervals, types of events (regular or haboob) and wind directions in the range 150–330 ° (a) and 330–150 ° (b). The number of available 15-min average PSDs in each u_* interval are indicated in the legend. Panels (c)-(d) are the same as (a)-(b) but normalized ($Norm.\ dM/dlnD_i$) after removing the anthropogenic mode (normalization from 0.37 to 19.11 µm). The insets show the same data but with logarithmic ordinate axis scaling. Shaded areas around the lines depict the standard error. The shown PSDs were obtained from FidasU. In (a) and (b) the dashed dark blue line marks the end of the anthropogenic mode ($D_i = 0.42\,\mu m$). In this case, the original size resolution of FidasU has been reduced by integrating 4 consecutive bins except for the last one that contains 3, resulting in 16 bins. The first integrated bin is not represented as Fidas is considered efficient from the second one onward.

S9 Additional figures related to the diffusive flux PSDs

Figs. S13 and S14 show the same plots as Figs. 8 and 9 but including the uncertainties for each u_* range only for the haboob events. We also provide the diffusive flux PSDs with uncertainties only accounting for standard errors (Figs. S15 and S16). As the standard error depends inversely on the number of samples, those cases in which there is only a sample do not show any shaded areas.

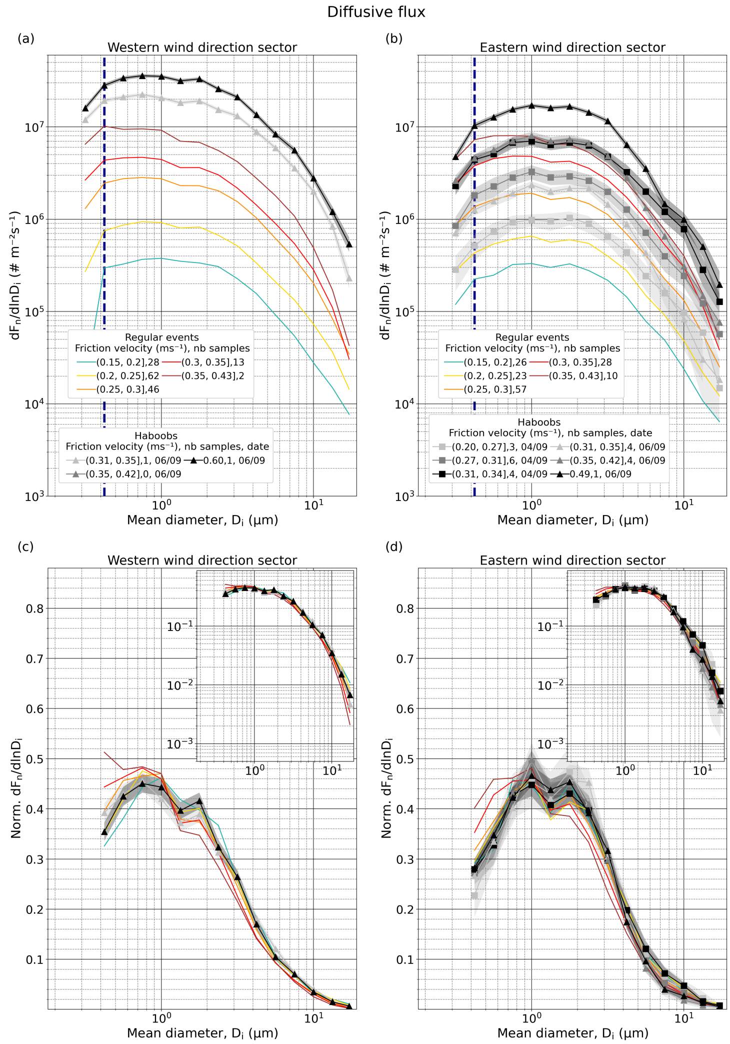

Figure S13. Average size-resolved number diffusive flux, $dF_n/dlnD_i$ ($\# \, \mathrm{m}^{-2}\,\mathrm{s}^{-1}$), for different u_* intervals, types of events (regular or haboob) and wind directions in the range 150–330 ° (a) and 330–150 ° (b). The number of available 15-min average PSDs in each u_* interval are indicated in the legend. Only the samples where flux is positive in all the diameter bins above the anthropogenic mode (as discussed in Sect. 3.3.1) have been selected. Panels (c)-(d) are the same as (a)-(b) but normalized ($Norm.\ dF_n/dlnD_i$) after removing the anthropogenic mode (normalization from 0.37 to 19.11 µm). The insets show the same data but with logarithmic ordinate axis scaling. Shaded areas around the lines of the haboob event PSDs depict the combination of random uncertainty and standard error. In (a) and (b) the dashed dark blue line marks the end of the anthropogenic mode ($D_i = 0.42\,\mu\mathrm{m}$). In this case, the original size resolution of FidasL has been reduced by integrating 4 consecutive bins except for the last one that contains 3, resulting in 16 bins. The first integrated bin is not represented as Fidas is considered efficient from the second one onward. Results are shown only for well-developed erosion conditions ($u_* > 0.15\,\mathrm{m\,s^{-1}}$).

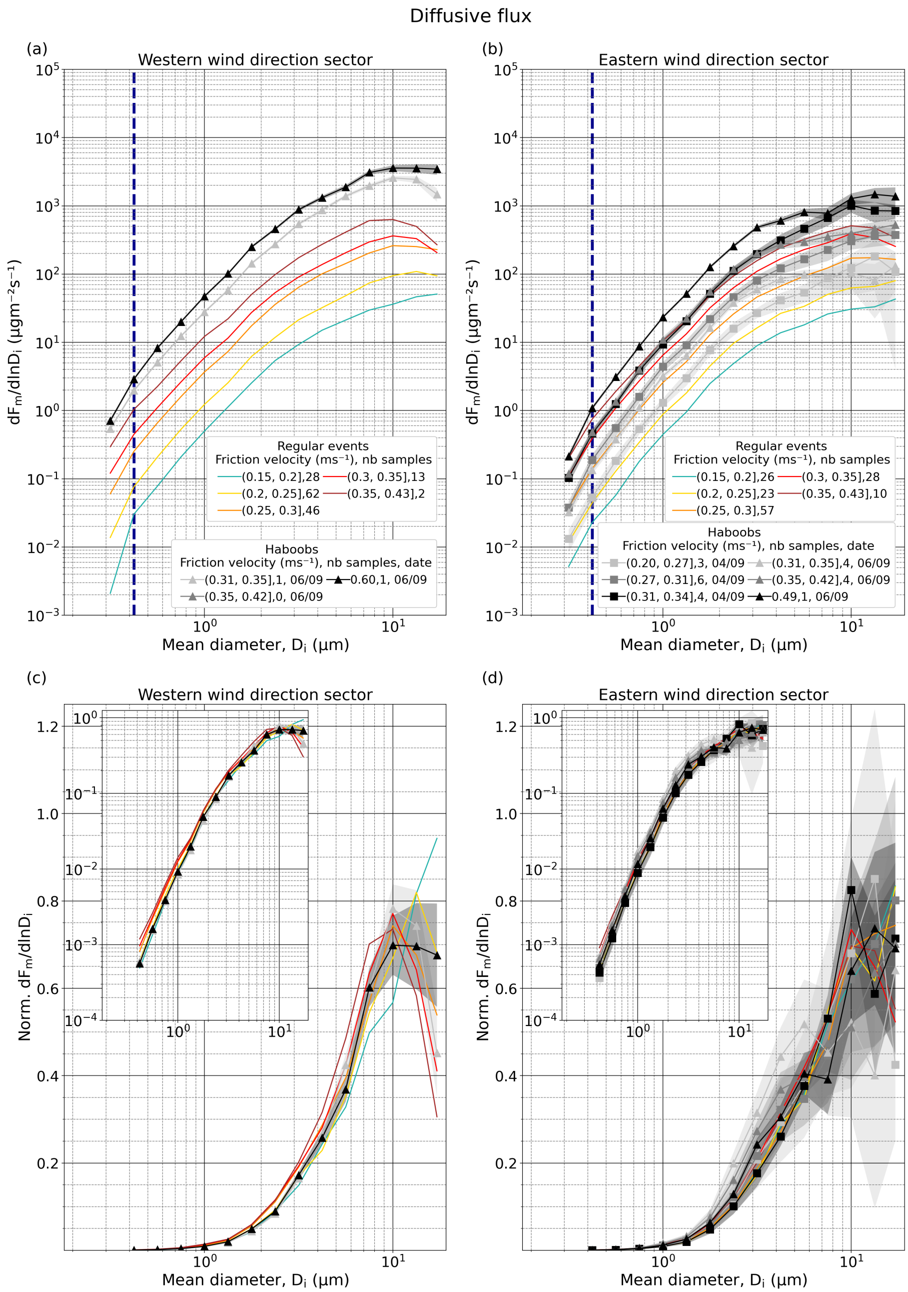

Figure S14. Average size-resolved mass diffusive flux, $dF_m/dlnD_i$ ($\mu g\, m^{-2}\, s^{-1}$), for different u_* intervals, types of events (regular or haboob) and wind directions in the range 150–330° (a) and 330–150° (b). The number of available 15-min average PSDs in each u_* class are indicated in the legend. Only the samples where diffusive flux is positive in all the diameter bins above the anthropogenic mode (as discussed in Sect. 3.3.1) have been selected. Panels (c)-(d) are the same as (a)-(b) but normalized ($Norm.\ dF_m/dlnD_i$) after removing the anthropogenic mode (normalization from 0.37 to 19.11 µm). The insets show the same data but with logarithmic ordinate axis scaling. Shaded areas around the lines of the haboob event PSDs depict the combination of random uncertainty and standard error. In (a) and (b) the dashed dark blue line marks the end of the anthropogenic mode ($D_i = 0.42\,\mu m$). In this case, the original size resolution of FidasL has been reduced by integrating 4 consecutive bins except for the last one that contains 3, resulting in 16 bins. The first integrated bin is not represented as Fidas is considered efficient from the second one onward. Results are shown only for well-developed erosion conditions (u_* > $0.15\, m\, s^{-1}$).

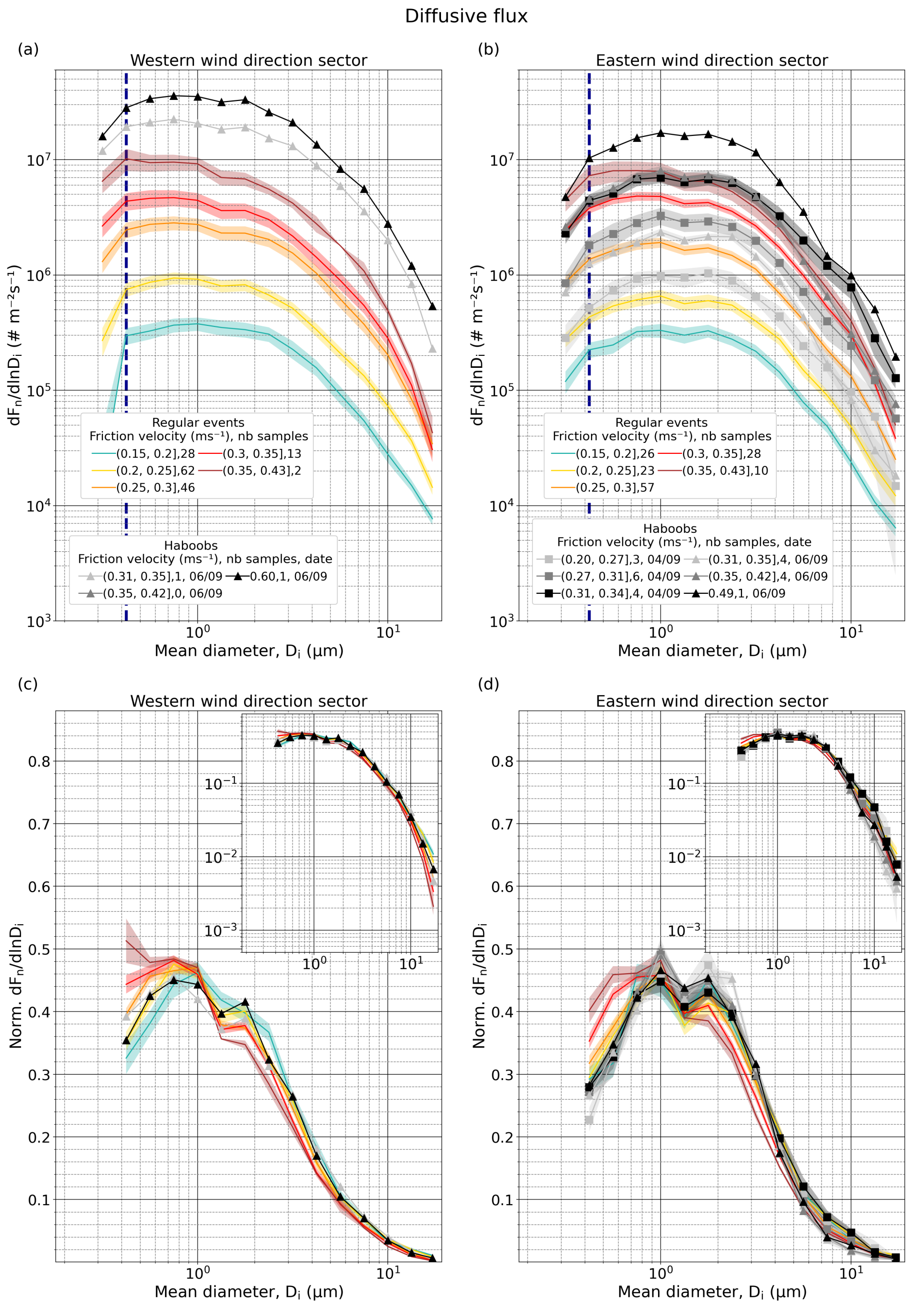

Figure S15. Average size-resolved number diffusive flux, $dF_n/dlnD_i$ ($\# \, \mathrm{m}^{-2}\,\mathrm{s}^{-1}$), for different u_* intervals, types of events (regular or haboob) and wind directions in the range 150–330 ° (a) and 330–150 ° (b). The number of available 15-min average PSDs in each u_* interval are indicated in the legend. Only the samples where diffusive flux is positive in all the diameter bins above the anthropogenic mode (as discussed in Sect. 3.3.1) have been selected. Panels (c)-(d) are the same as (a)-(b), but normalized ($Norm.\ dF_n/dlnD_i$) after removing the anthropogenic mode (normalization from 0.37 to 19.11 µm). The insets show the same data, but with logarithmic ordinate axis scaling. Shaded areas around the lines depict the standard error. In (a) and (b) the dashed dark blue line marks the end of the anthropogenic mode ($D_i = 0.42\,\mu\mathrm{m}$). In this case, the original size resolution of FidasL has been reduced by integrating 4 consecutive bins except for the last one that contains 3, resulting in 16 bins. The first integrated bin is not represented as Fidas is considered efficient from the second one onward. Results are shown only for well-developed erosion conditions ($u_* > 0.15\,\mathrm{m\,s^{-1}}$).

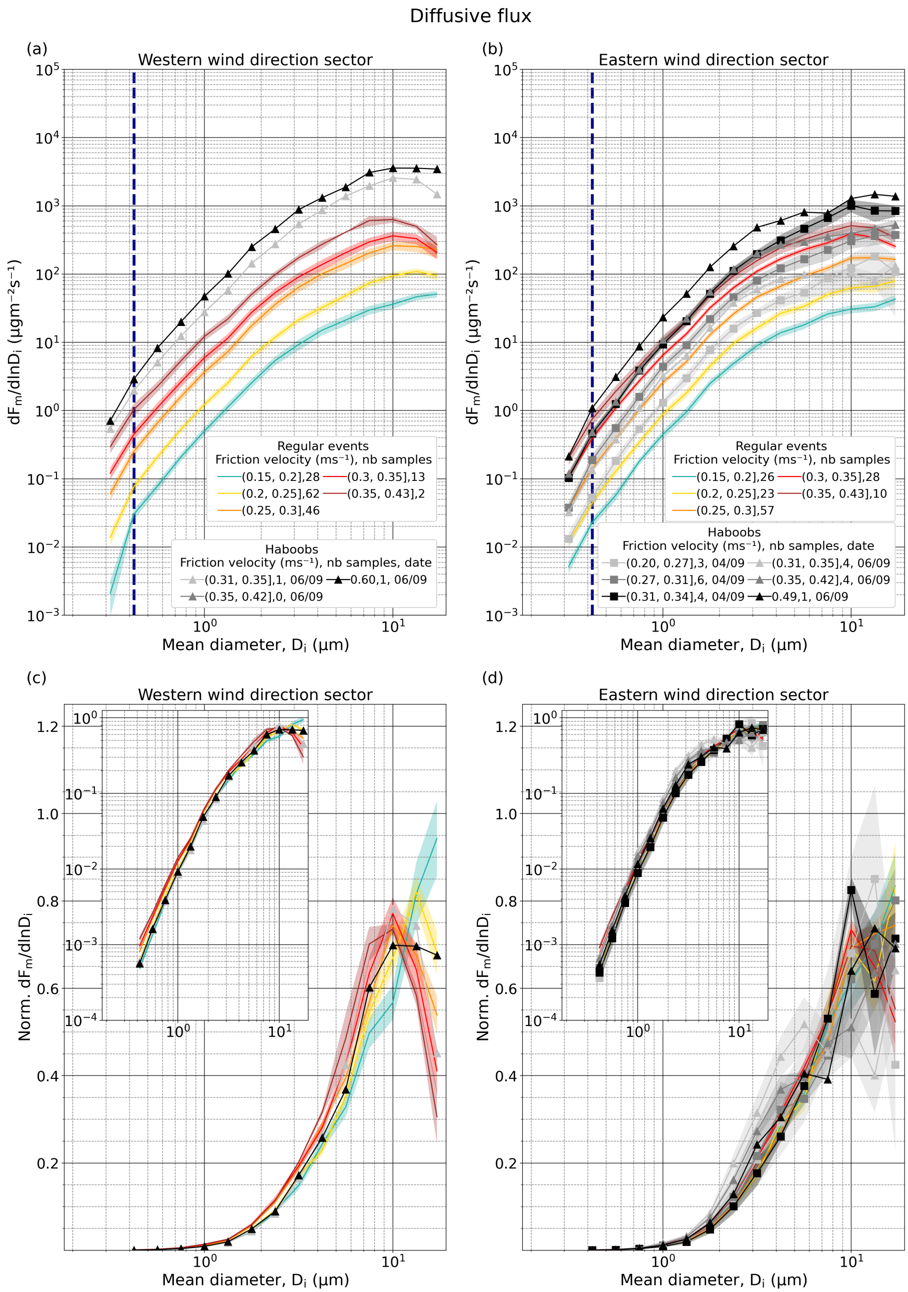

Figure S16. Average size-resolved mass diffusive flux, $dF_m/dlnD_i$ ($\mu g\,m^{-2}\,s^{-1}$), for different u_* intervals, types of events (regular or haboob) and wind directions in the range 150–330° (a) and 330–150° (b). The number of available 15-min average PSDs in each u_* class are indicated in the legend. Only the samples where diffusive flux is positive in all the diameter bins above the anthropogenic mode (as discussed in Sect. 3.3.1) have been selected. Panels (c)-(d) are the same as (a)-(b) but normalized ($Norm.\ dF_m/dlnD_i$) after removing the anthropogenic mode (normalization from 0.37 to 19.11 µm). The insets show the same data but with logarithmic ordinate axis scaling. Shaded areas around the lines depict the standard error. In (a) and (b) the dashed dark blue line marks the end of the anthropogenic mode ($D_i = 0.42\,\mu m$). In this case, the original size resolution of FidasL has been reduced by integrating 4 consecutive bins except for the last one that contains 3, resulting in 16 bins. First integrated bin is not represented as Fidas is considered efficient from the second one onward. Results are shown only for well-developed erosion conditions ($u_* > 0.15\,m\,s^{-1}$).

S10 Additional figures related to the dry deposition velocity

Measurements of dry deposition velocity v_{dep} close to dust source regions are not very frequent (Marticorena et al., 2017; Bergametti et al., 2018). Fig. S17 displays our observation-based v_{dep} inferred as described in Sect. 2.4 for different u_* intervals, along with the experimental data from Bergametti et al. (2018) (magenta points) and the estimated v_{dep} applying F19 (dashed line), Z01 (solid line) and the tuned parameterization (dashdot line). For the tuned configuration we set $B_1 = 0.02$, $d_c = 0.0009\,\mathrm{m}$ and $A_{in} = 15$.

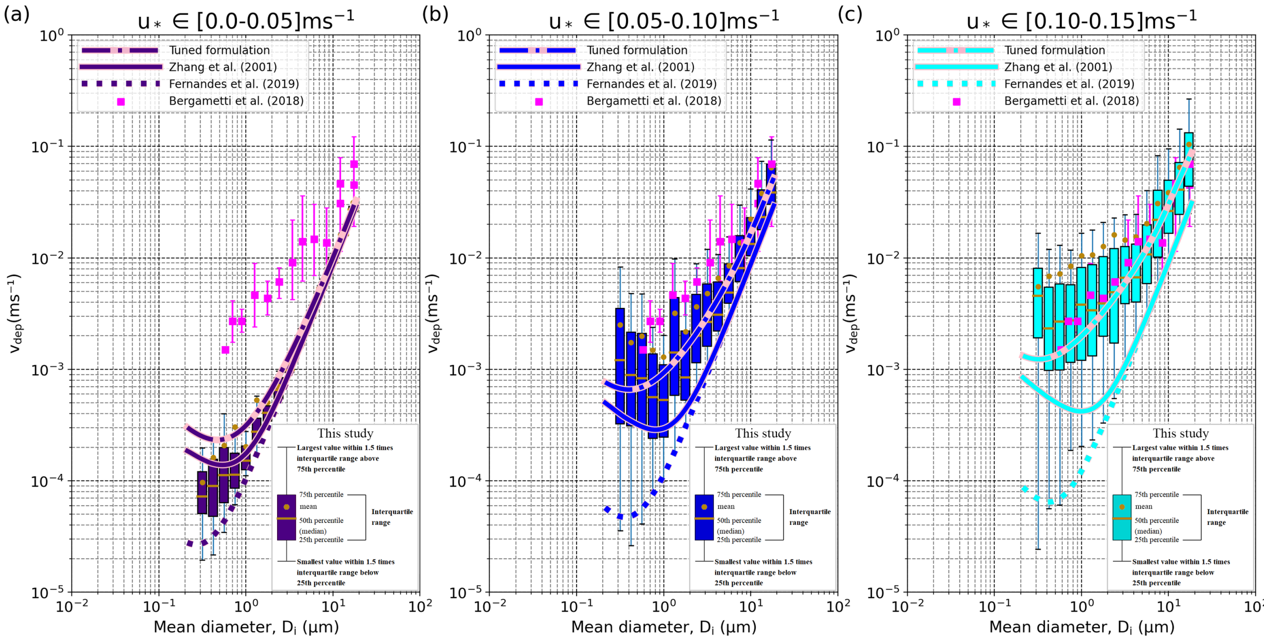

Figure S17. In situ size-resolved measurements of dry deposition velocity $v_{dep}(\mathrm{m\,s^{-1}})$ for u_* between (a) (0 – 0.05) $\mathrm{m\,s^{-1}}$, (b) (0.05 – 0.10) $\mathrm{m\,s^{-1}}$ and (c) (0.10 – 0.15) $\mathrm{m\,s^{-1}}$ (bar plots). Lines represent the estimated median v_{dep} applying F19 (dashed), Z01 (solid) and the tuned parameterization (dashdot) for the corresponding u_* interval. The points in magenta represent the measurements from Bergametti et al. (2018).

Fig. S18 shows the sensitivity of the tuned parameterization used to estimate v_{dep} (described in Appendix D) to different values of A_{in}, B_1 and d_c. The separation between curves for particles with fine, intermediate and coarse diameters is mostly controlled by the variation in A_{in}, B_1 and d_c, respectively.

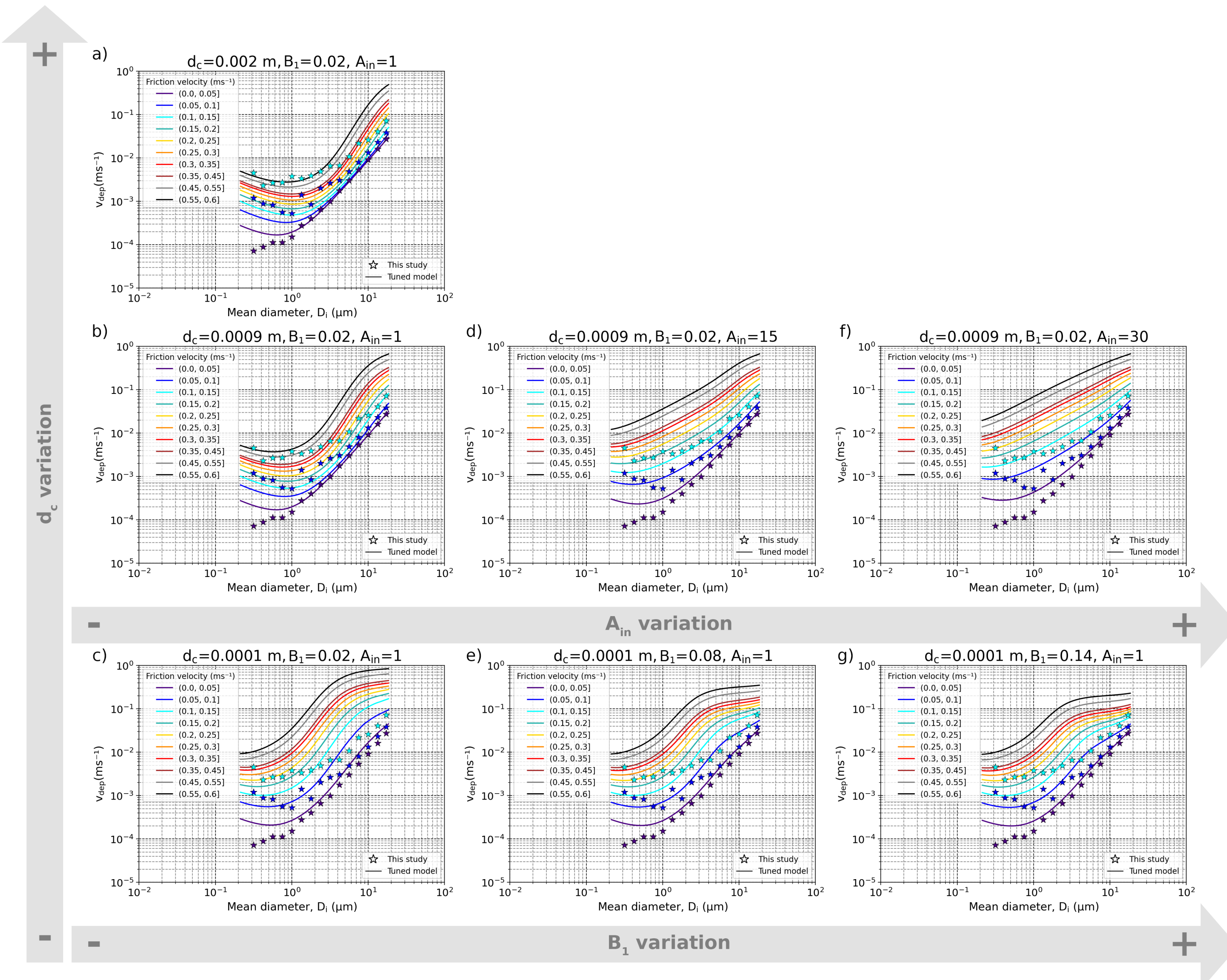

Figure S18. Different configurations of the tuned parameterization for estimating v_{dep} applying different values of A_{in}, B_1 and d_c.

S11 Dry deposition fluxes

Figs. S19 and S20 represent, respectively, the number and mass dry deposition fluxes calculated in absolute terms as $|F_{dep}(D_i)| = v_{dep}(D_i)c_{int}$ for different u_* intervals, types of events (regular and haboob events) and wind direction (Eastern and Western sectors) using the tuned parameterization for v_{dep} ($B_1 = 0.02$, $d_c = 0.0009\,\mathrm{m}$ and $A_{in} = 15$). Analogous plots are obtained using F19 (Figs. S21 and S22) and Z01 (Figs. S23 and S24). Significant higher values of dry deposition fluxes are obtained when using the tuned parameterization, reaching values above $10^7\,\#\,\mathrm{m}^{-2}\,\mathrm{s}^{-1}$ in terms of number and $10^3\,\mu\mathrm{g}\,\mathrm{m}^{-2}\,\mathrm{s}^{-1}$ in mass, compared to F19 and Z01. Also the shape of the curves changes considerably between the different schemes.

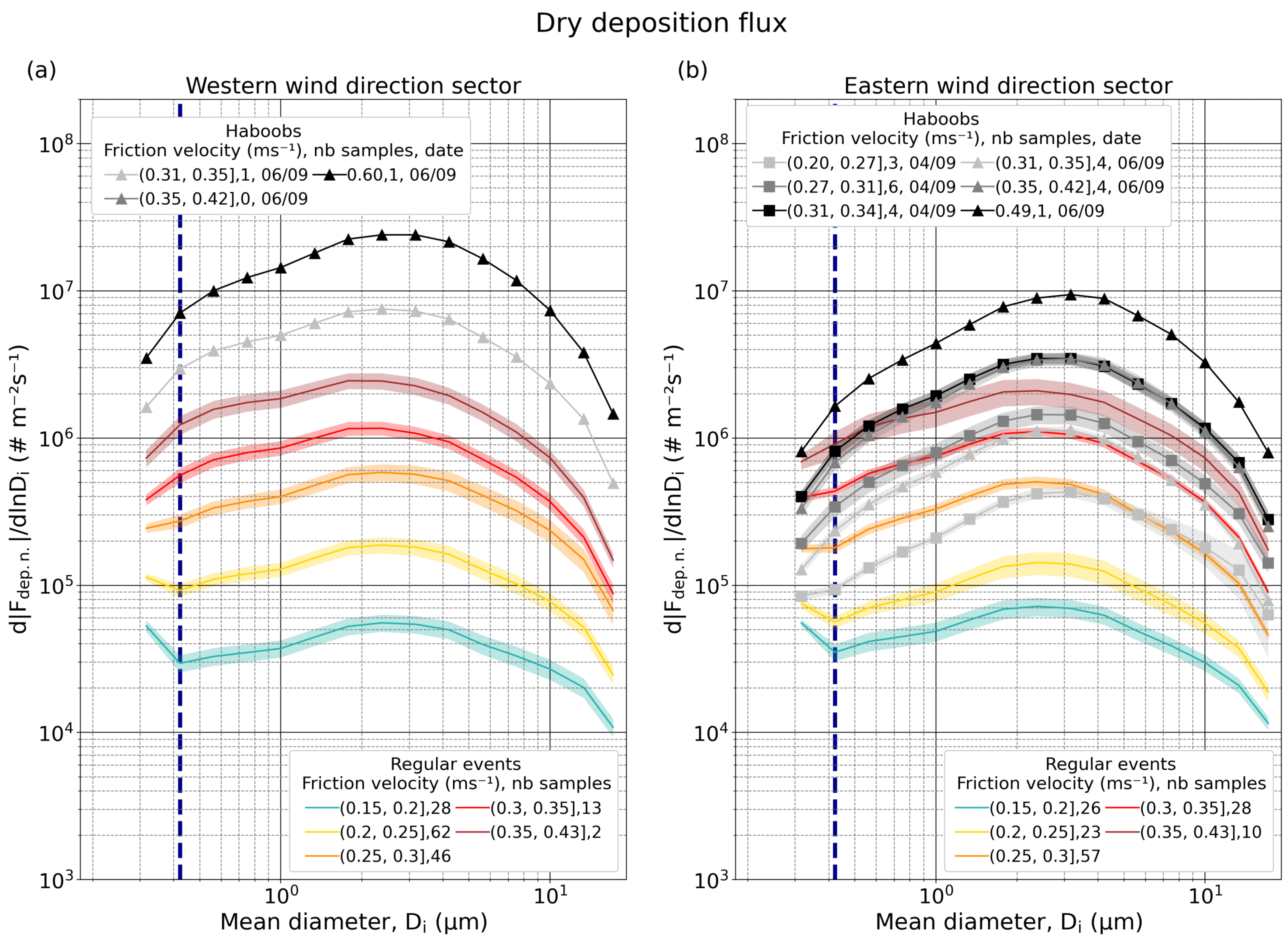

Figure S19. Average size-resolved number dry deposition flux, $d|F_{dep.n}|/dlnD_i$ ($\#\,\mathrm{m}^{-2}\,\mathrm{s}^{-1}$), estimated from the v_{dep} tuned formulation for different u_* intervals, types of events (regular or haboob) and wind directions in the range 150–330° (a) and 330–150° (b). Only the samples where diffusive flux is positive in all the diameter bins above the anthropogenic mode (as discussed in Sect. **??**) have been selected. The number of available 15-min average PSDs in each u_* interval are indicated in the legend. Shaded areas around the lines depict the standard error. In (a) and (b) the dashed dark blue line marks the end of the anthropogenic mode ($D_i = 0.42\,\mu\mathrm{m}$). In this case, the original size resolution of FidasL has been reduced by integrating 4 consecutive bins except for the last one that contains 3, resulting in 16 bins. The first integrated bin is not represented as the Fidas is considered efficient from the second one onward.

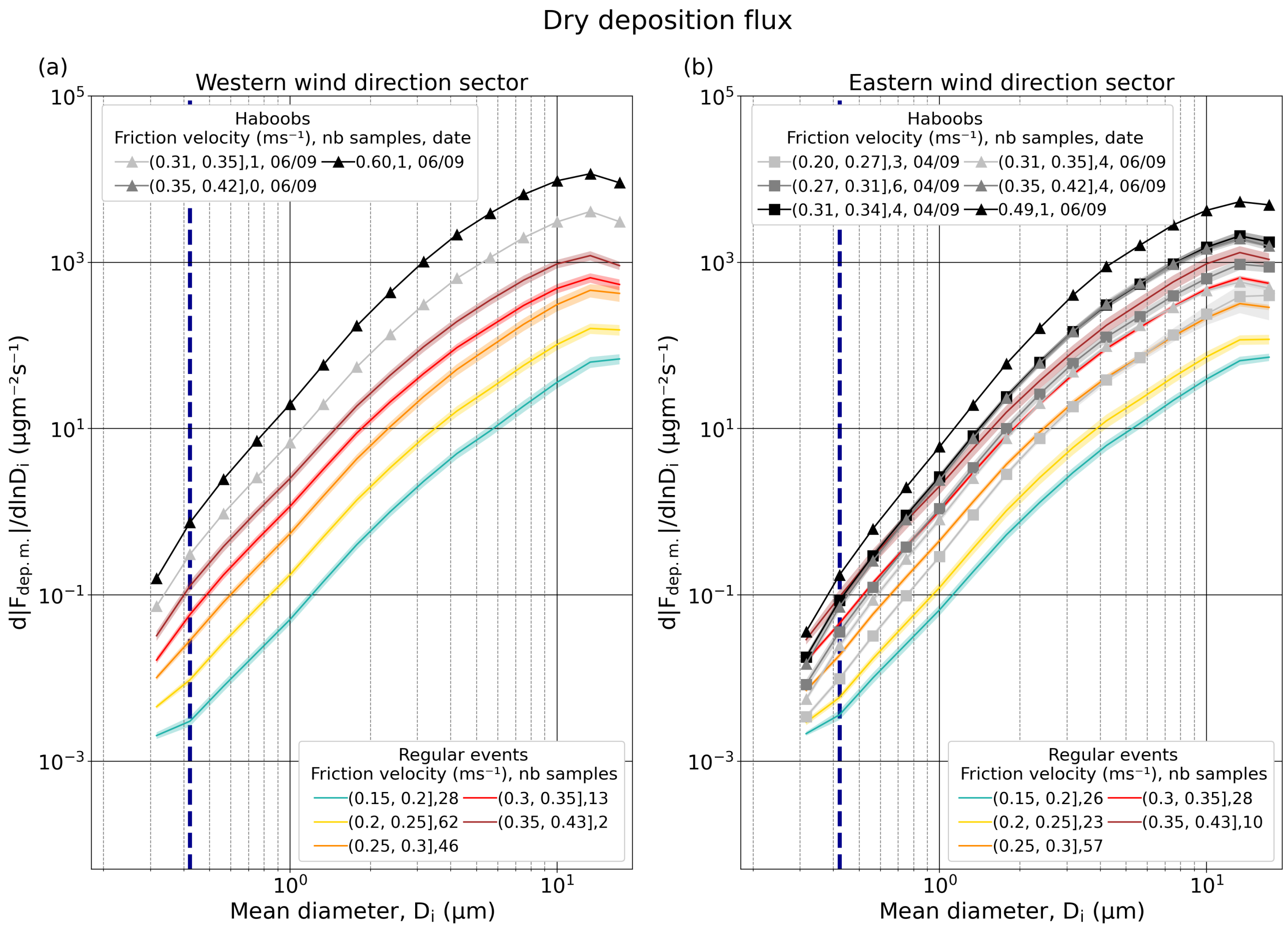

Figure S20. Average size-resolved mass dry deposition flux, $d|F_{dep.m}|/dlnD_i$ ($\mu\text{g}\,\text{m}^{-2}\,\text{s}^{-1}$), estimated from the v_{dep} tuned formulation for different u_* intervals, types of events (regular or haboob) and wind directions in the range 150–330° (a) and 330–150° (b). Only the samples where diffusive flux is positive in all the diameter bins above the anthropogenic mode (as discussed in Sect. **??**) have been selected. The number of available 15-min average PSDs in each u_* interval are indicated in the legend. Shaded areas around the lines depict the standard error. In (a) and (b) the dashed dark blue line marks the end of the anthropogenic mode ($D_i = 0.42\,\mu\text{m}$). In this case, the original size resolution of FidasL has been reduced by integrating 4 consecutive bins except for the last one that contains 3, resulting in 16 bins. The first integrated bin is not represented as the Fidas is considered efficient from the second one onward.

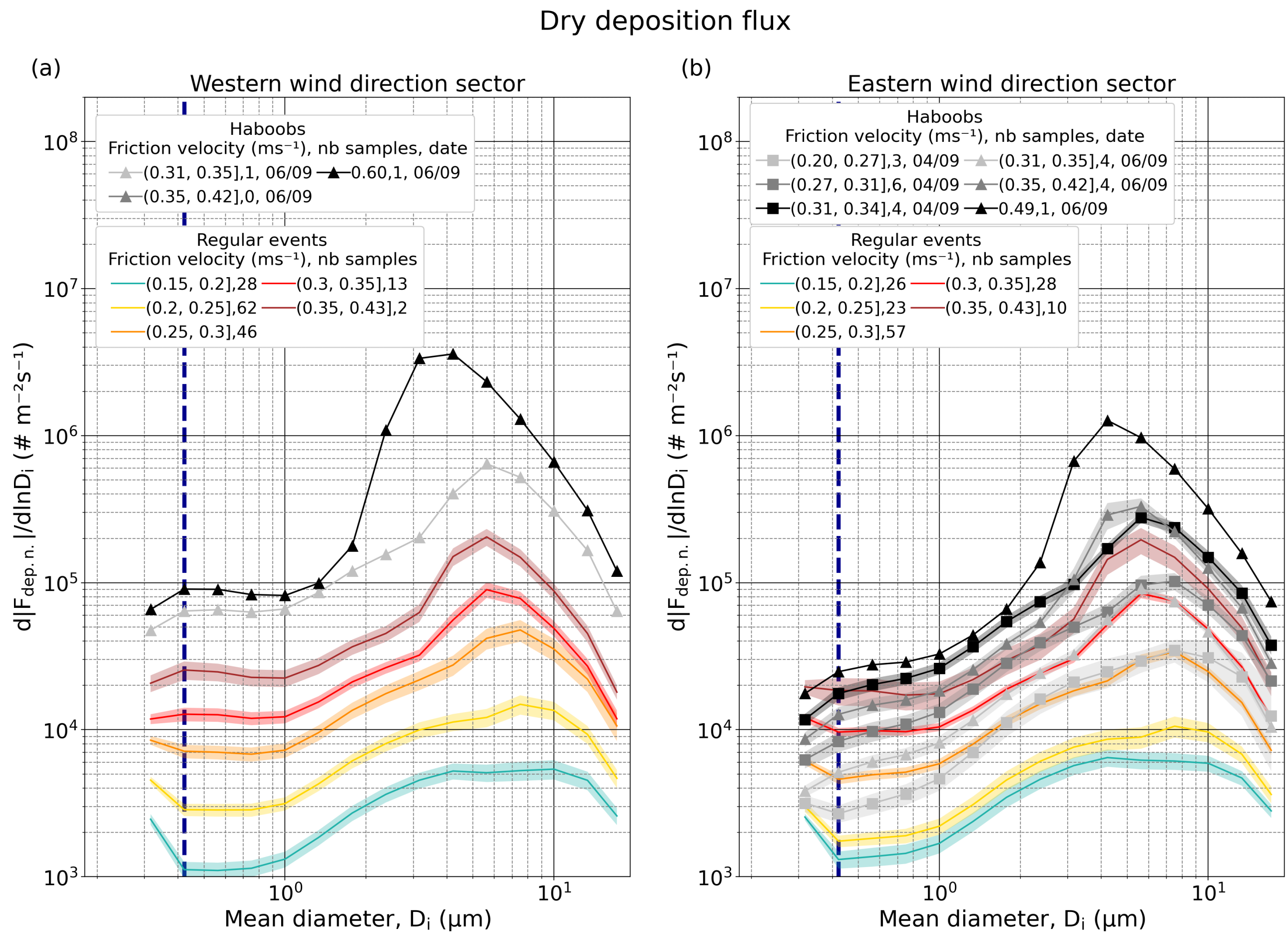

Figure S21. Average size-resolved number dry deposition flux, $d|F_{dep.n}|/dlnD_i$ ($\#\,\mathrm{m}^{-2}\,\mathrm{s}^{-1}$), estimated from the v_{dep} F19 for different u_* intervals, types of events (regular or haboob) and wind directions in the range 150–330 ° (a) and 330–150 ° (b). Only the samples where diffusive flux is positive in all the diameter bins above the anthropogenic mode (as discussed in Sect. **??**) have been selected. The number of available 15-min average PSDs in each u_* interval are indicated in the legend. Shaded areas around the lines depict the standard error. In (a) and (b) the dashed dark blue line marks the end of the anthropogenic mode ($D_i = 0.42\,\mu\mathrm{m}$). In this case, the original size resolution of FidasL has been reduced by integrating 4 consecutive bins except for the last one that contains 3, resulting in 16 bins. The first integrated bin is not represented as the Fidas is considered efficient from the second one onward.

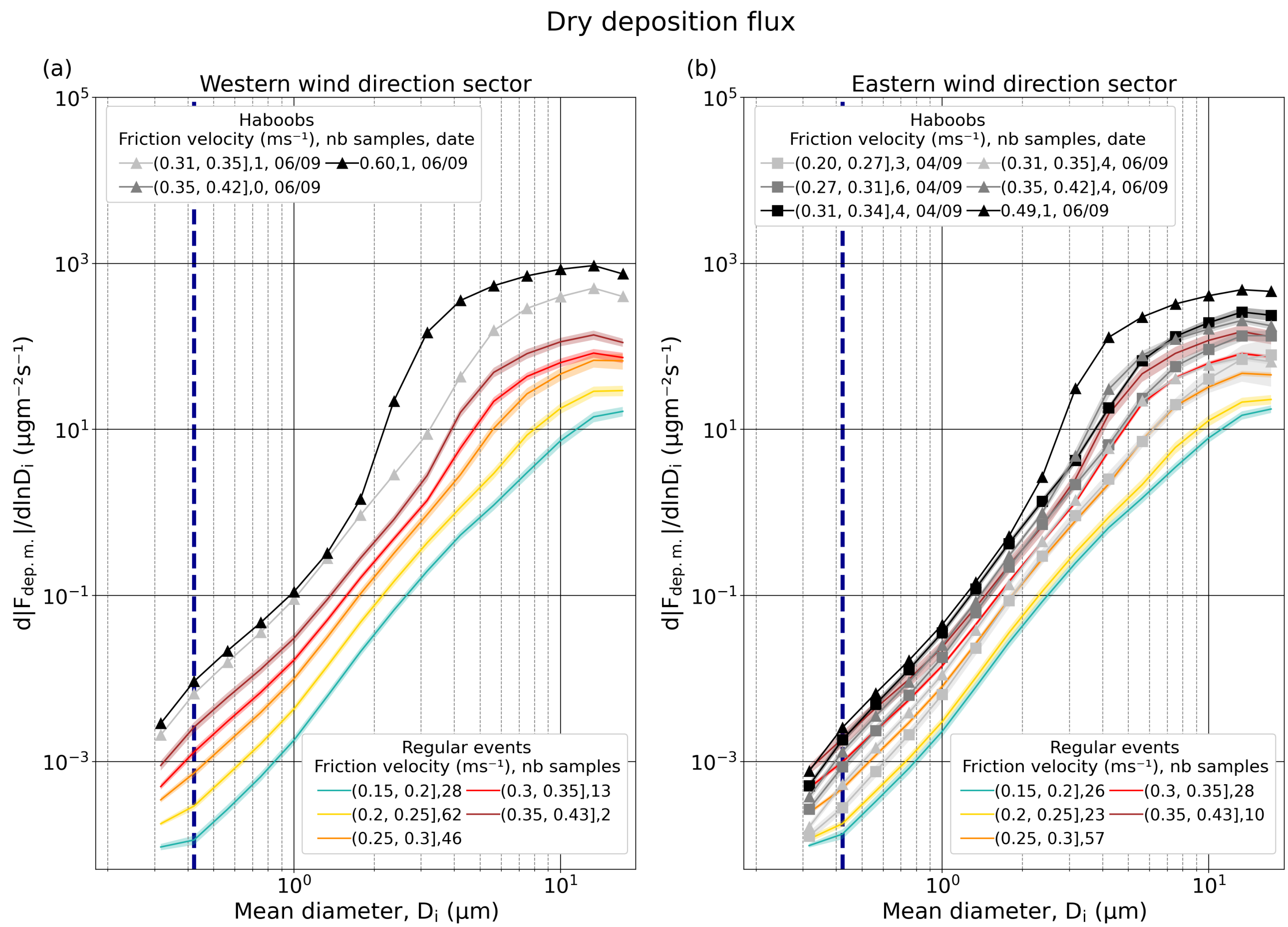

Figure S22. Average size-resolved mass dry deposition flux, $d|F_{dep.m}|/dlnD_i$ ($\mu g\,m^{-2}\,s^{-1}$), estimated from the v_{dep} F19 for different u_* intervals, types of events (regular or haboob) and wind directions in the range 150–330 $^\circ$ (a) and 330–150 $^\circ$ (b). Only the samples where diffusive flux is positive in all the diameter bins above the anthropogenic mode (as discussed in Sect. **??**) have been selected. The number of available 15-min average PSDs in each u_* interval are indicated in the legend. Shaded areas around the lines depict the standard error. In (a) and (b) the dashed dark blue line marks the end of the anthropogenic mode ($D_i = 0.42\,\mu m$). In this case, the original size resolution of FidasL has been reduced by integrating 4 consecutive bins except for the last one that contains 3, resulting in 16 bins. The first integrated bin is not represented as the Fidas is considered efficient from the second one onward.

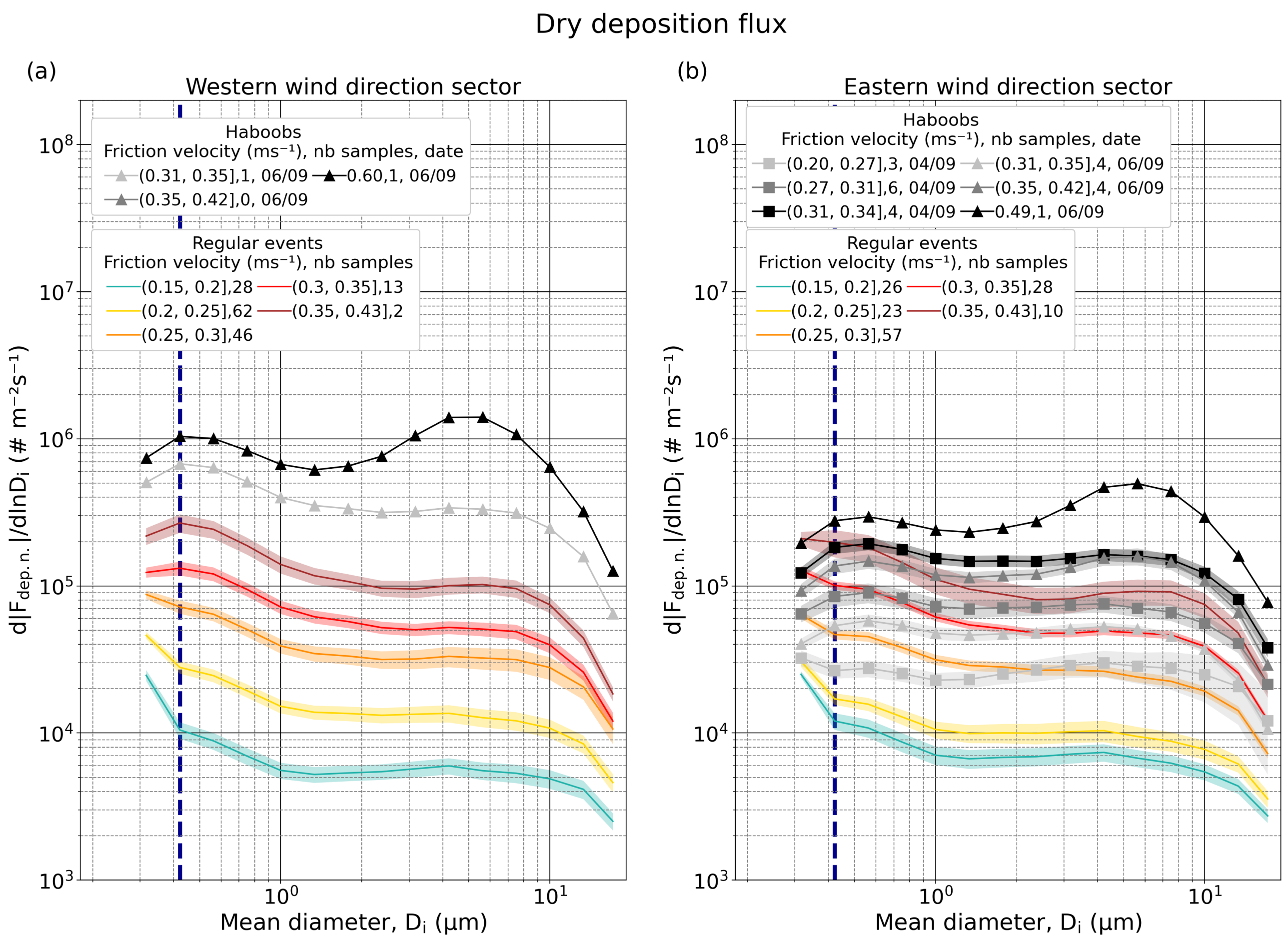

Figure S23. Average size-resolved number dry deposition flux, $d|F_{dep.n}|/dlnD_i$ ($\# \, \mathrm{m}^{-2} \, \mathrm{s}^{-1}$), estimated from the v_{dep} Z01 for different u_* intervals, types of events (regular or haboob) and wind directions in the range 150–330 ° (a) and 330–150 ° (b). Only the samples where diffusive flux is positive in all the diameter bins above the anthropogenic mode (as discussed in Sect. **??**) have been selected. The number of available 15-min average PSDs in each u_* interval are indicated in the legend. Shaded areas around the lines depict the standard error. In (a) and (b) the dashed dark blue line marks the end of the anthropogenic mode ($D_i = 0.42 \, \mu\mathrm{m}$). In this case, the original size resolution of FidasL has been reduced by integrating 4 consecutive bins except for the last one that contains 3, resulting in 16 bins. The first integrated bin is not represented as the Fidas is considered efficient from the second one onward.

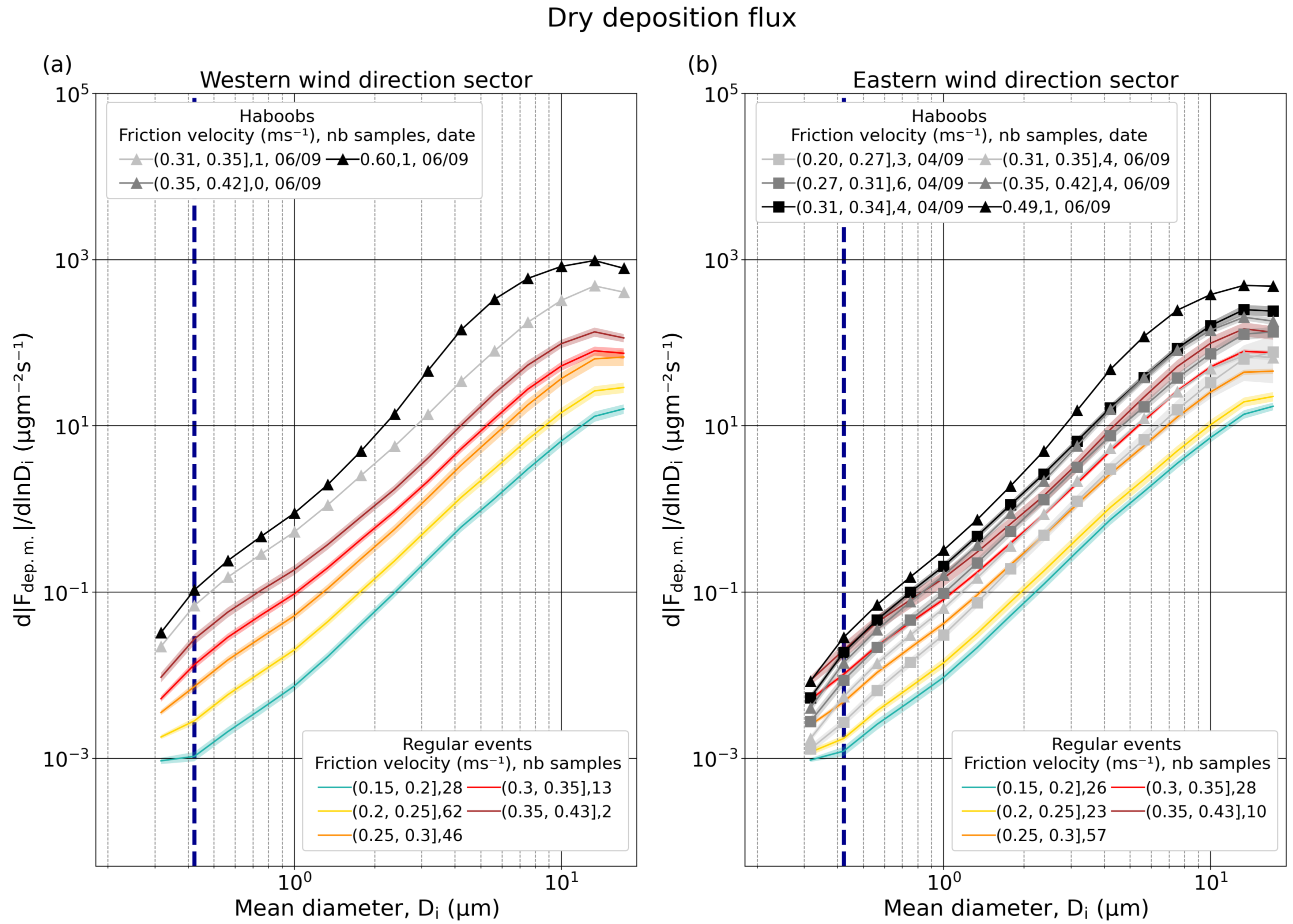

Figure S24. Average size-resolved mass dry deposition flux, $d|F_{dep.m}|/dlnD_i$ ($\mu g\,m^{-2}\,s^{-1}$), estimated from the v_{dep} Z01 for different u_* intervals, types of events (regular or haboob) and wind directions in the range 150–330° (a) and 330–150° (b). Only the samples where diffusive flux is positive in all the diameter bins above the anthropogenic mode (as discussed in Sect. **??**) have been selected. The number of available 15-min average PSDs in each u_* interval are indicated in the legend. Shaded areas around the lines depict the standard error. In (a) and (b) the dashed dark blue line marks the end of the anthropogenic mode ($D_i = 0.42\,\mu m$). In this case, the original size resolution of FidasL has been reduced by integrating 4 consecutive bins except for the last one that contains 3, resulting in 16 bins. The first integrated bin is not represented as the Fidas is considered efficient from the second one onward.

S12 Additional figures related to the estimated emitted flux PSDs

Fig. S25 shows the number normalized and non-normalized estimated emitted flux PSDs, calculated following Eq. 12 and using the tuned formulation for v_{dep}, for each u_* range. The uncertainties (combination of random uncertainty and standard error) are shown only for the regular events for the sake of clarity. Compared to the diffusive flux (see Appendix C) there is an extra source of uncertainty for the estimated emitted flux, the v_{dep}. However, as we only have observation-based v_{dep} for the first three u_* intervals (see Sects. 2.4 and S14) we can not estimate its uncertainty for the rest of the u_* intervals. Dry deposition parameterizations like the ones used (Zhang et al., 2001; Fernandes et al., 2019) are likely afflicted with large structural uncertainties as evidenced when compared with observations, therefore are not used to estimate the uncertainty. Future work may explore the use of other deposition models that better fit our measurements, but is out of the scope of this paper and for this reason we neglect the uncertainty of v_{dep}. So, as for the diffusive flux, we estimate the uncertainty of the estimated emitted flux assuming the FidasL as the reference device, correcting the systematic deviation of the FidasU and only propagating the random uncertainty as:

$$\sigma_{F_{emi}(D_i)} = u_* \kappa \frac{\sigma_{c_u(D_i)}}{\ln\left(\frac{z_u}{z_l}\right) - \Psi_m\left(\frac{z_u}{L}\right) + \Psi_m\left(\frac{z_l}{L}\right)} + \frac{v_{dep}(D_i) - v_g(D_i)}{2}\sigma_{c_u(D_i)} \tag{1}$$

where we have taken into account that $c_{int}(D_i) = (c_u(D_i) + c_l(D_i))/2$, being $c_u(D_i)$ the FidasU concentrations after systematic correction and $c_l(D_i)$ FidasL concentration and thus, the uncertainty in the estimated emitted flux $\sigma_{F_{emi}(D_i)}$ only depends on the uncertainty of the FidasU concentration with respect to the FidasL concentration $\sigma_{c_u(D_i)}$. Finally, the average total uncertainty for each u_* interval is calculated as the square root of the quadratic sum of the standard error of the estimated emitted flux and the average estimated emitted flux uncertainty within each u_* interval. The average estimated emitted flux uncertainty is calculated analogously to Eq. 11, but for the estimated emitted flux.

We also provide the estimated emitted flux PSDs obtained using the dry deposition from F19 (Figs. S26 and S27) and Z01 (Figs. S28 and S29). Compared to the diffusive flux, the estimated emitted dust flux shows a higher proportion of particles in all size bins, but specially significant for coarse and super-coarse particles (Figs. 11a, 11b, S25a and S25b). However, this increase is very subtle, almost unnoticed in logarithmic scale, when applying F19 (Figs. S26a, S26b, S27a and S27b) and Z01 (Figs. S28a, S28b, S29a and S29b), in agreement with the smaller dry deposition fluxes (see Sect. S11).

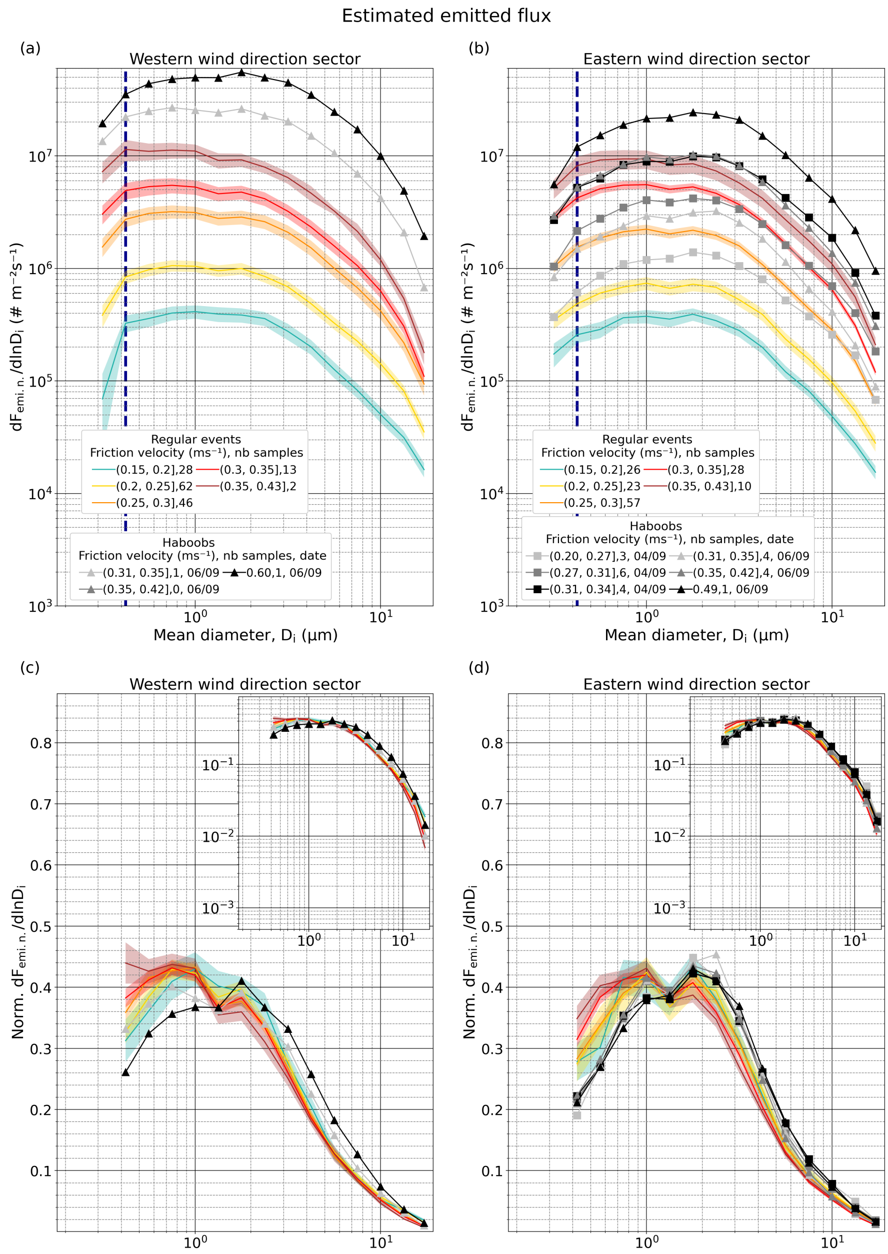

Figure S25. Average size-resolved number estimated emitted flux, $dF_{emi.n}/dlnD_i$ ($\#\,\mathrm{m}^{-2}\,\mathrm{s}^{-1}$) from the tuned v_{dep} parameterization, for different u_* intervals, types of events (regular or haboob) and wind directions in the range 150–330° (a) and 330–150° (b). The number of available 15-min average PSDs in each u_* interval are indicated in the legend. Only the samples where diffusive flux is positive in all the diameter bins above the anthropogenic mode (as discussed in Sect. 3.3.1) have been selected. Panels (c)-(d) are the same as (a)-(b) but normalized ($Norm.\ dF_{emi.n}/dlnD_i$) after removing the anthropogenic mode (normalization from 0.37 to 19.11 µm). The insets show the same data but with logarithmic ordinate axis scaling. Shaded areas around the lines of the regular event PSDs depict the combination of random uncertainty and standard error. In (a) and (b) the dashed dark blue line marks the end of the anthropogenic mode ($D_i = 0.42\,\mu\mathrm{m}$). In this case, the original size resolution of FidasL has been reduced by integrating 4 consecutive bins except for the last one that contains 3, resulting in 16 bins. The first integrated bin is not represented as Fidas is considered efficient from the second one onward. Results are shown only for well-developed erosion conditions ($u_* > 0.15\,\mathrm{m\,s^{-1}}$).

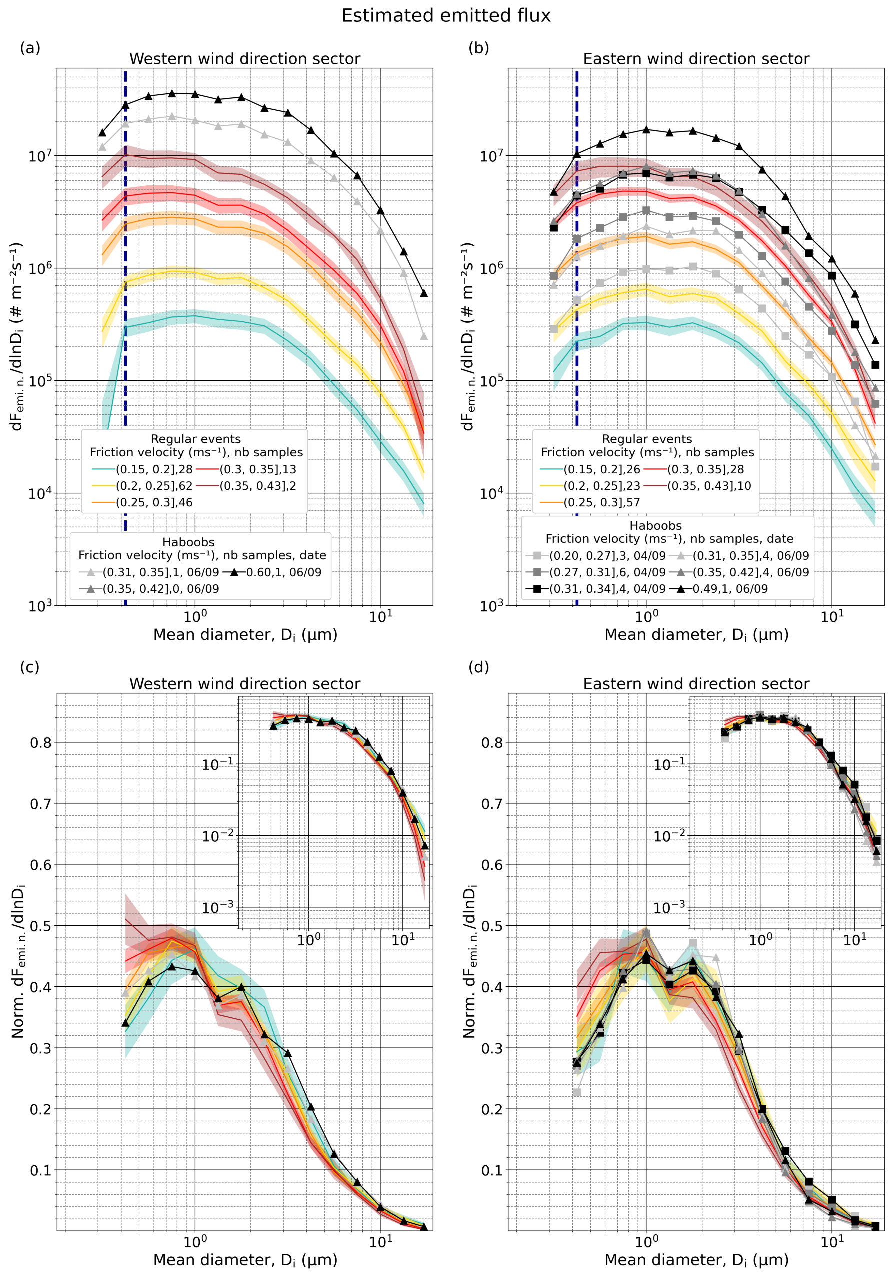

Figure S26. Average size-resolved number estimated emitted flux, $dF_{emi.n}/dlnD_i$ ($\#\,\mathrm{m}^{-2}\,\mathrm{s}^{-1}$) using F19 for v_{dep} calculation, for different u_* intervals, types of events (regular or haboob) and wind directions in the range 150–330 $^\circ$ (a) and 330–150 $^\circ$ (b). The number of available 15-min average PSDs in each u_* interval are indicated in the legend. Only the samples where diffusive flux is positive in all the diameter bins above the anthropogenic mode (as discussed in Sect. 3.3.1) have been selected. Panels (c)-(d) are the same as (a)-(b) but normalized ($Norm.\ dF_{emi.n}/dlnD_i$) after removing the anthropogenic mode (normalization from 0.37 to 19.11 µm). The insets show the same data but with logarithmic ordinate axis scaling. Shaded areas around the lines of the regular event PSDs depict the combination of random uncertainty and standard error. In (a) and (b) the dashed dark blue line marks the end of the anthropogenic mode ($D_i = 0.42\,\mu\mathrm{m}$). In this case, the original size resolution of FidasL has been reduced by integrating 4 consecutive bins except for the last one that contains 3, resulting in 16 bins. The first integrated bin is not represented as Fidas is considered efficient from the second one onward. Results are shown only for well-developed erosion conditions ($u_* > 0.15\,\mathrm{m\,s^{-1}}$).

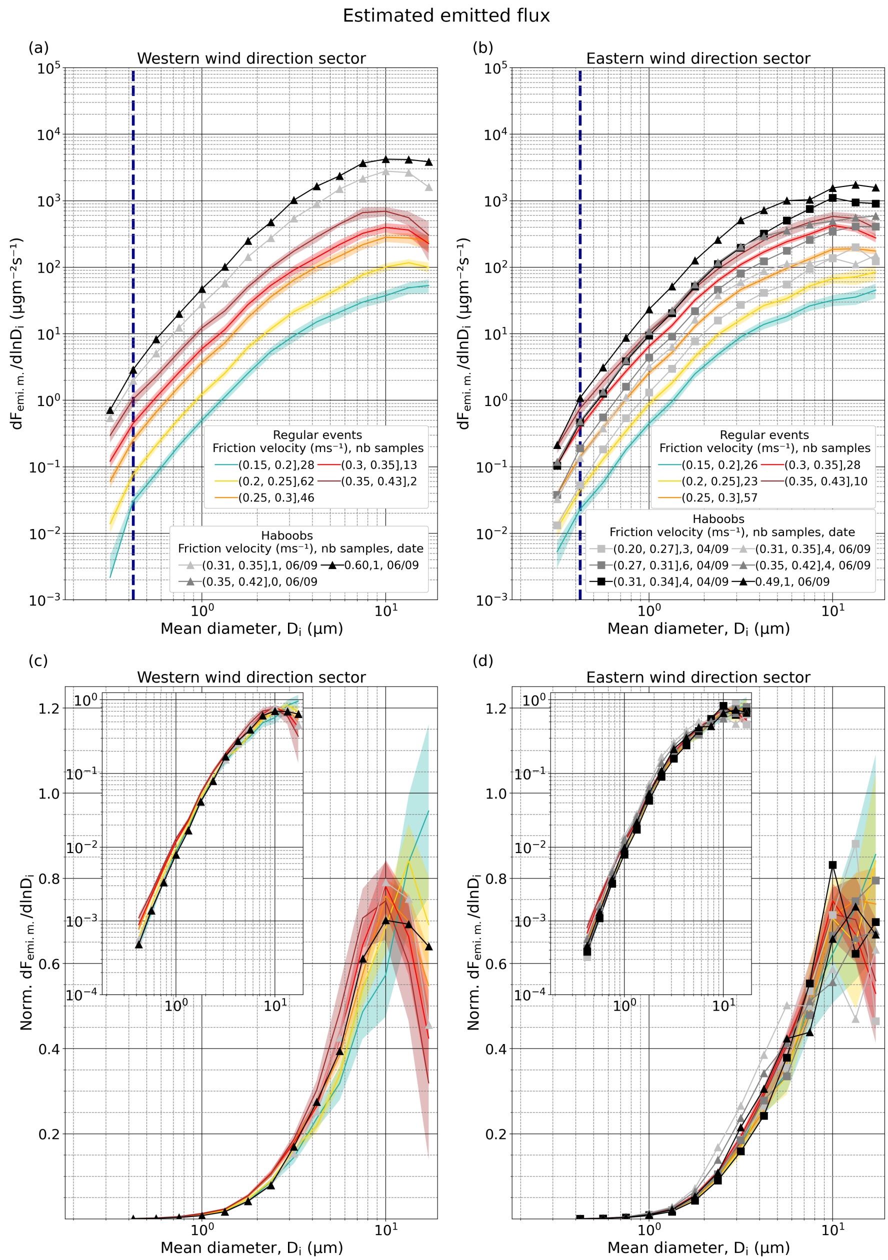

Figure S27. Average size-resolved mass estimated emitted flux, $dF_{emi.m}/dlnD_i$ ($\mu g\,m^{-2}\,s^{-1}$) using F19 for v_{dep} calculation, for different u_* intervals, types of events (regular or haboob) and wind directions in the range 150–330 ° (a) and 330–150 ° (b). The number of available 15-min average PSDs in each u_* class are indicated in the legend. Only the samples where diffusive flux is positive in all the diameter bins above the anthropogenic mode (as discussed in Sect. 3.3.1) have been selected. Panels (c)-(d) are the same as (a)-(b) but normalized ($Norm.\ dF_{emi.m}/dlnD_i$) after removing the anthropogenic mode (normalization from 0.37 to 19.11 µm). The insets show the same data, but with logarithmic ordinate axis scaling. Shaded areas around the lines of the haboob event PSDs depict the combination of random uncertainty and standard error. In (a) and (b) the dashed dark blue line marks the end of the anthropogenic mode ($D_i = 0.42\,\mu m$). In this case, the original size resolution of FidasL has been reduced by integrating 4 consecutive bins except for the last one that contains 3, resulting in 16 bins. The first integrated bin is not represented as Fidas is considered efficient from the second one onward. Results are shown only for well-developed erosion conditions ($u_* > 0.15\,m\,s^{-1}$).

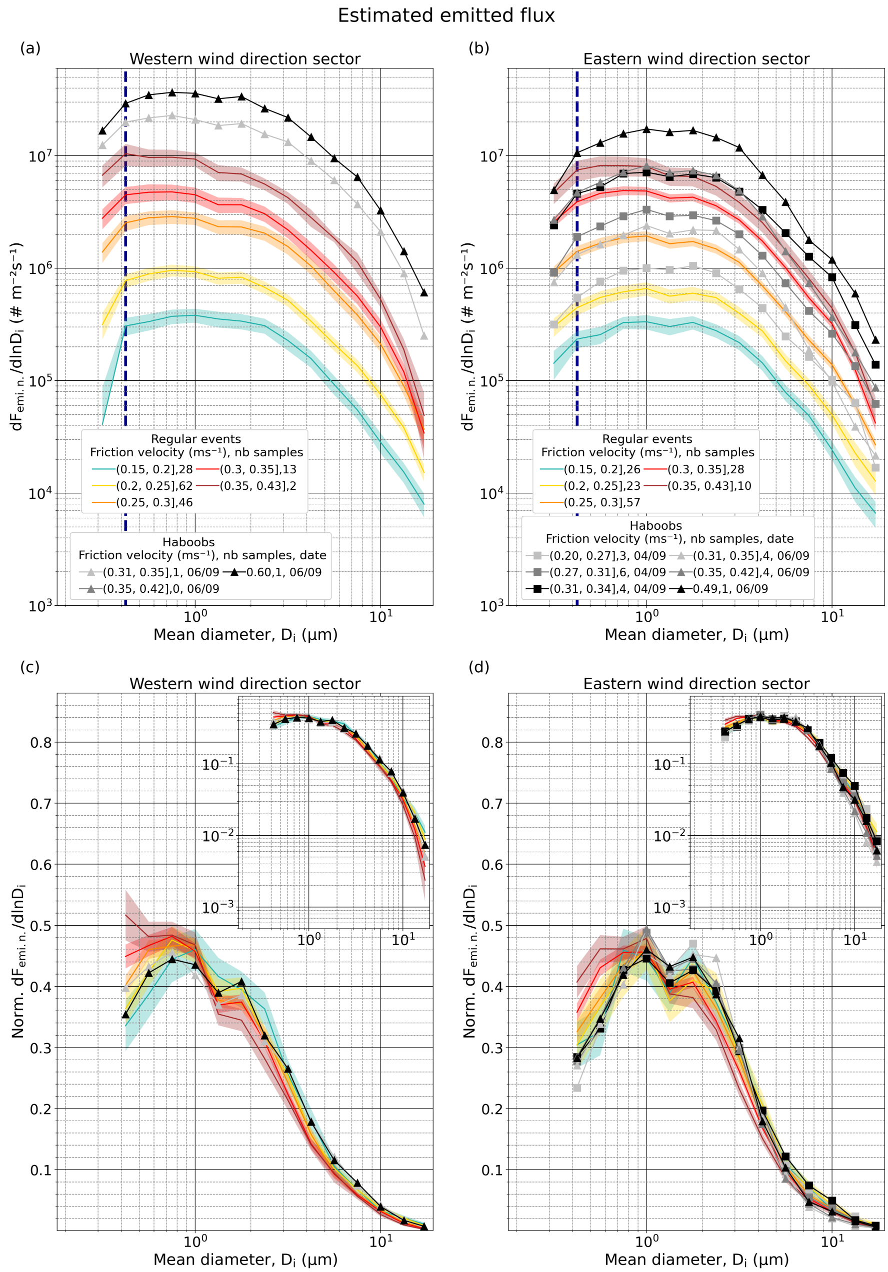

Figure S28. Average size-resolved number estimated emitted flux, $dF_{emi.n}/dlnD_i$ ($\#\,\mathrm{m}^{-2}\,\mathrm{s}^{-1}$) using Z01 for v_{dep} calculation, for different u_* intervals, types of events (regular or haboob) and wind directions in the range 150–330° (a) and 330–150° (b). The number of available 15-min average PSDs in each u_* interval are indicated in the legend. Only the samples where diffusive flux is positive in all the diameter bins above the anthropogenic mode (as discussed in Sect. 3.3.1) have been selected. Panels (c)-(d) are the same as (a)-(b) but normalized ($Norm.\ dF_{emi.n}/dlnD_i$) after removing the anthropogenic mode (normalization from 0.37 to 19.11 µm). The insets show the same data but with logarithmic ordinate axis scaling. Shaded areas around the lines of the regular event PSDs depict the combination of random uncertainty and standard error. In (a) and (b) the dashed dark blue line marks the end of the anthropogenic mode ($D_i = 0.42\,\mu\mathrm{m}$). In this case, the original size resolution of FidasL has been reduced by integrating 4 consecutive bins except for the last one that contains 3, resulting in 16 bins. First integrated bin is not represented as Fidas is considered efficient from the second one onward. Results are shown only for well-developed erosion conditions ($u_* > 0.15\,\mathrm{m\,s}^{-1}$).

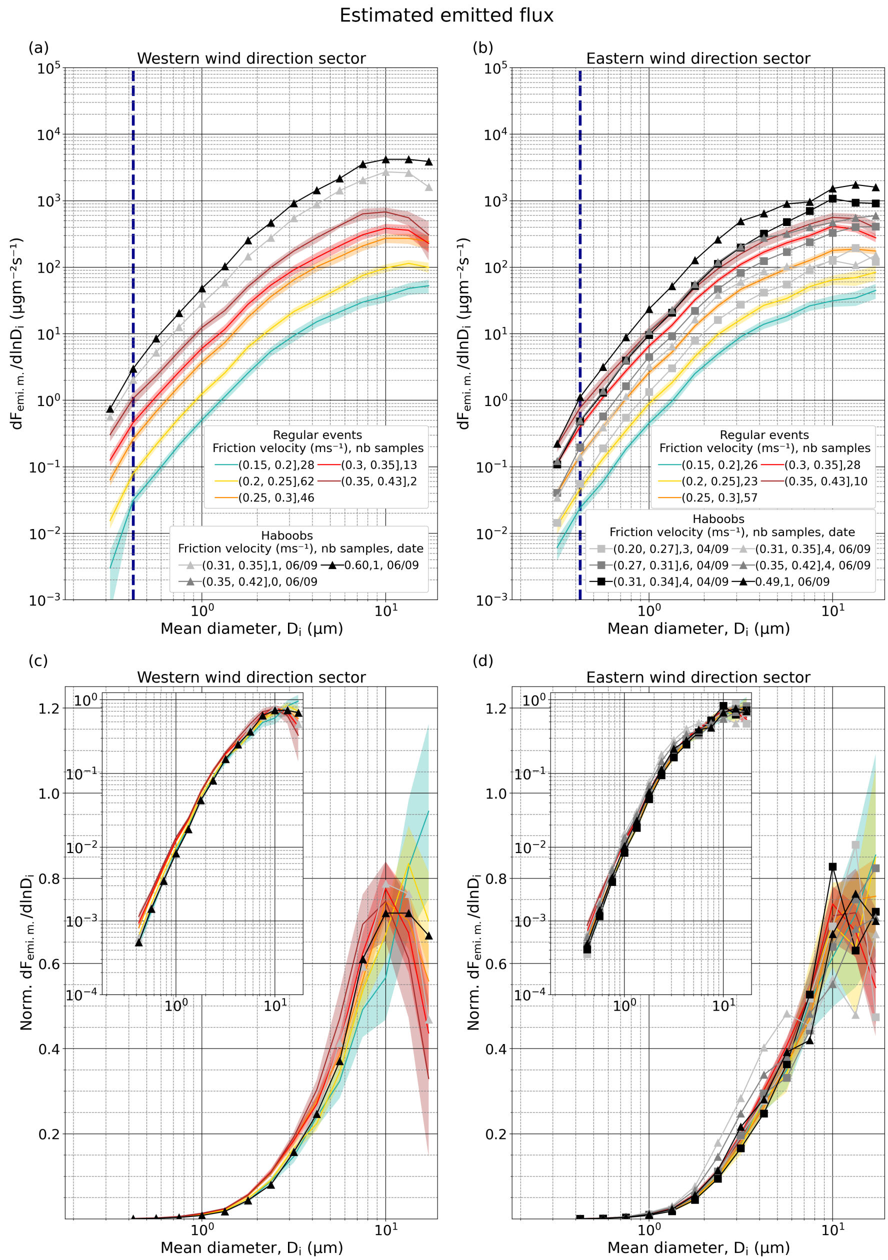

Figure S29. Average size-resolved mass estimated emitted flux, $dF_{emi.m}/dlnD_i$ ($\mu g\,m^{-2}\,s^{-1}$) using Z01 for v_{dep} calculation, for different u_* intervals, types of events (regular or haboob) and wind directions in the range 150–330 ° (a) and 330–150 ° (b). The number of available 15-min average PSDs in each u_* class are indicated in the legend. Only the samples where diffusive flux is positive in all the diameter bins above the anthropogenic mode (as discussed in Sect. 3.3.1) have been selected. Panels (c)-(d) are the same as (a)-(b) but normalized ($Norm.\ dF_{emi.m}/dlnD_i$) after removing the anthropogenic mode (normalization from 0.37 to 19.11 µm). The insets show the same data but with logarithmic ordinate axis scaling. Shaded areas around the lines of the haboob event PSDs depict the combination of random uncertainty and standard error. In (a) and (b) the dashed dark blue line marks the end of the anthropogenic mode ($D_i = 0.42\,\mu m$). In this case, the original size resolution of FidasL has been reduced by integrating 4 consecutive bins except for the last one that contains 3, resulting in 16 bins. The first integrated bin is not represented as Fidas is considered efficient from the second one onward. Results are shown only for well-developed erosion conditions ($u_* > 0.15\,m\,s^{-1}$).

S13 Nb and mass diffusive and estimated emitted flux fractions per diameter range and u_* interval

Figure S30 displays the number and mass fractions of diffusive flux between $\sim 0.37 < D_i < 1\,\mu\text{m}$, $\sim 1 < D_i < 2.5\,\mu\text{m}$, $\sim 2.5 < D_i < 10\,\mu\text{m}$ and $D_i > 10\,\mu\text{m}$ as a function of u_* for the two wind sectors and type of event (regular or haboob), calculated from the average values of the corresponding size integrated bins of each fraction for each u_* interval (Figs. 8a, 8b, 9a and 9b). The uncertainty of each fraction for each u_* interval is determined as the ratio between the square root of the quadratic sum of all the errors of the corresponding bins belonging to that fraction and the sum of the diffusive flux of all the bins with $D_i > 0.37\,\mu\text{m}$. As a reminder, the error of the diffusive flux for each bin is calculated combining the random uncertainty and standard error (see Appendix C and Sect. 2.3.2 for more details).

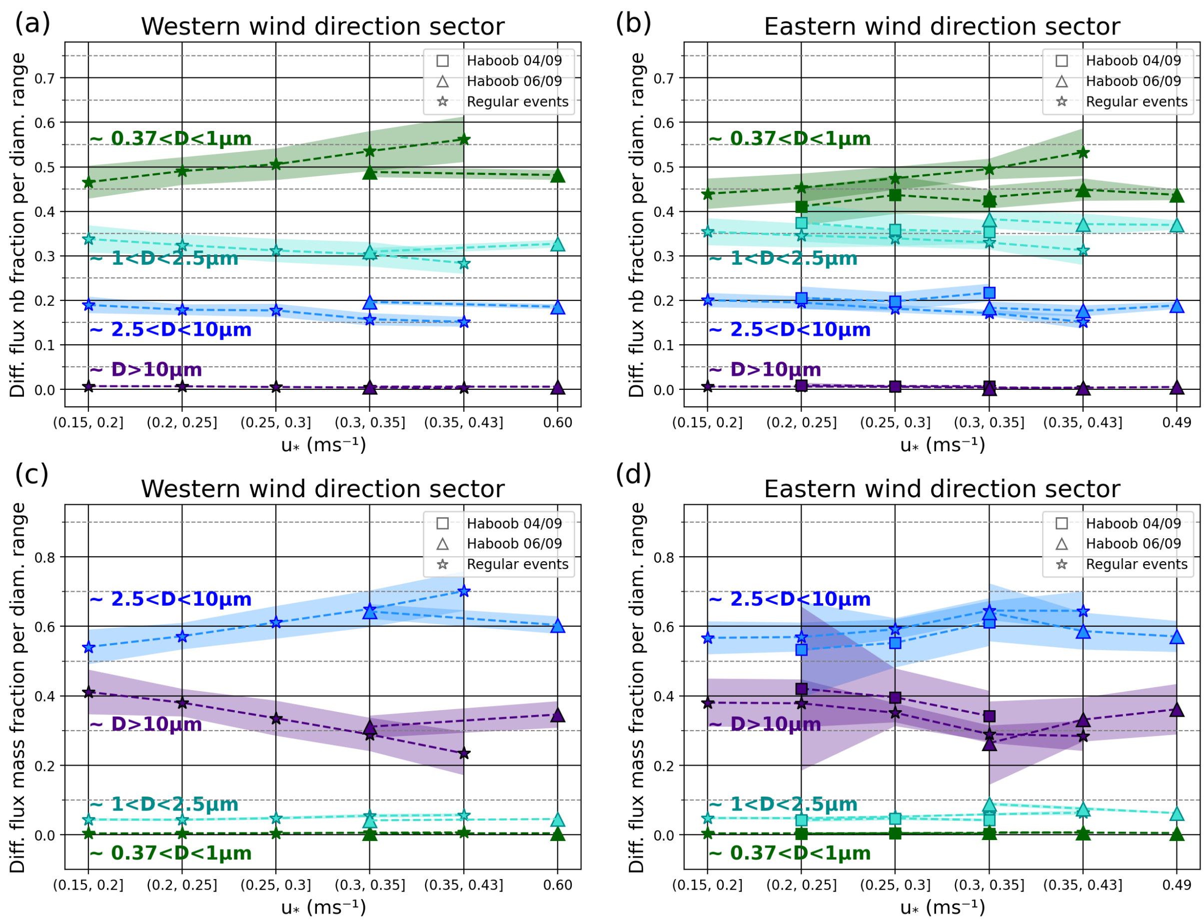

Figure S30. Number and mass diffusive flux fractions for different u_* intervals, types of events (regular or haboob) and wind directions in the range 150–330 ° (a-c) and 330–150°(b-d)

To analyze if the differences in the diffusive flux PSDs both between wind sectors and between u_* intervals were statistically significant we performed one-tailed tests of significance (Gorgas et al., 2011). This test allows evaluating if the mean of a population is statistically higher than the mean of another population. In our case we consider that: 1) our populations follow a normal distribution, 2) their variance are unknown, 3) the sum of the number of samples from each population is above 30 and 4) the number of samples of both populations is similar. Following these assumptions we use the test statistic z which follows a normal distribution and is defined as:

$$z = \frac{\overline{x_1} - \overline{x_2}}{\sqrt{\frac{s_1^2}{n_1} + \frac{s_2^2}{n_2})}} \quad (2)$$

where $\overline{x_i}$, s_i and n_i represent the mean, variance and number of samples of each population i. The null hypothesis H_0, defined as the contrary of what our data show, is accepted if $z \leq z_\alpha$ and rejected if $z > z_\alpha$, where the significance level α is 0.05.

This test is applied both considering certain fractions of diffusive flux (Fig. S30) and considering individually certain integrated size bins (Figs. 8c, 8d, 9c and 9d) (see Sect. 3.3.2).

Figure S31 is analogous to Fig. S30 but for the estimated emitted flux using the tuned formulation for v_{dep}. The tests of significance described above were also applied for the estimated emitted flux (see Sect. 3.5).

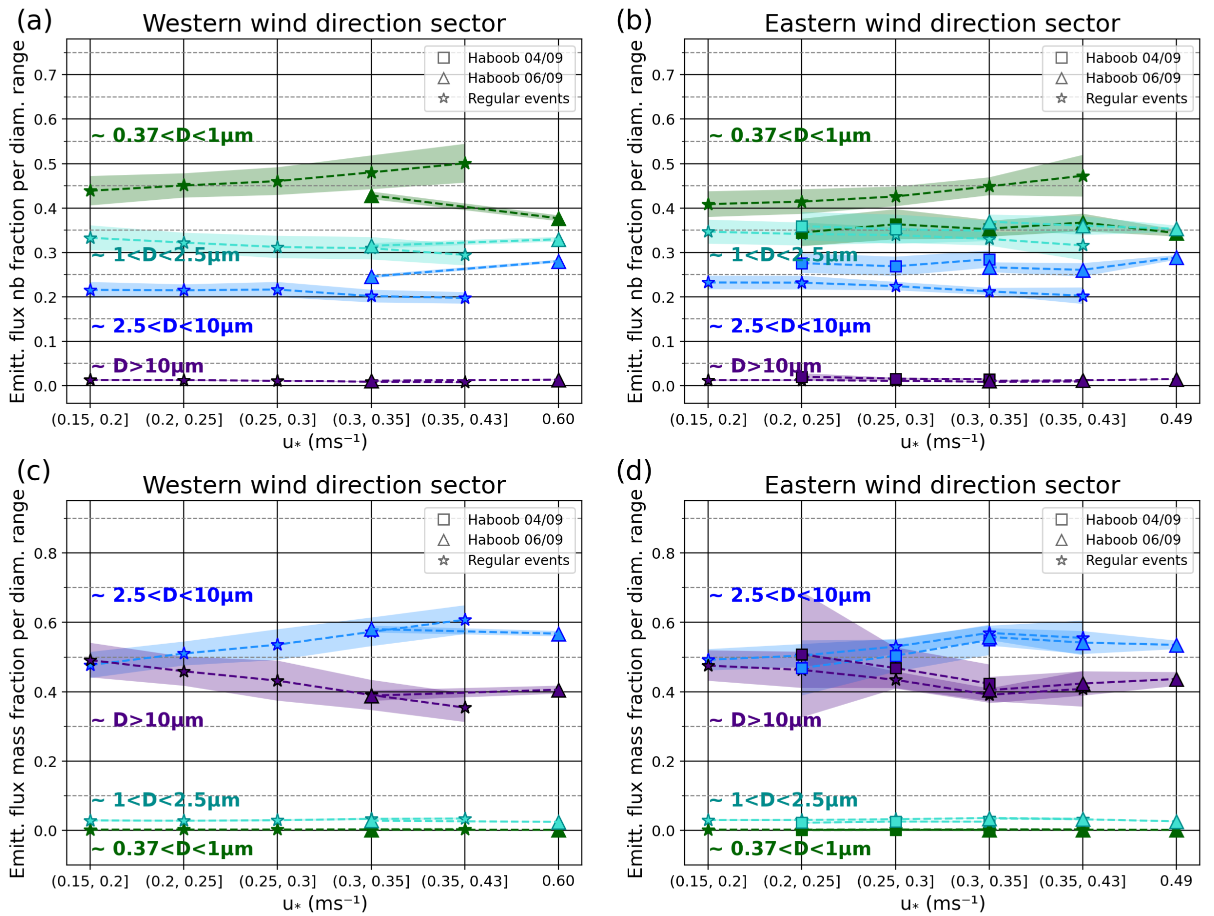

Figure S31. Number and mass emitted flux fractions for different u_* intervals, types of events (regular or haboob) and wind directions in the range 150–330 ° (a-c) and 330–150°(b-d)

S14 Ratio of dry deposition flux to the estimated emitted flux

Fig. S32 shows the size-resolved ratio of the dry deposition flux to the estimated emitted flux, determined using the v_{dep} tuned parameterization, for different u_* intervals, types of events and wind sectors. Analogous plots are obtained applying F19 (Fig. S33) and Z01 (Fig. S34). Much lower ratios are obtained for F19 and Z01.

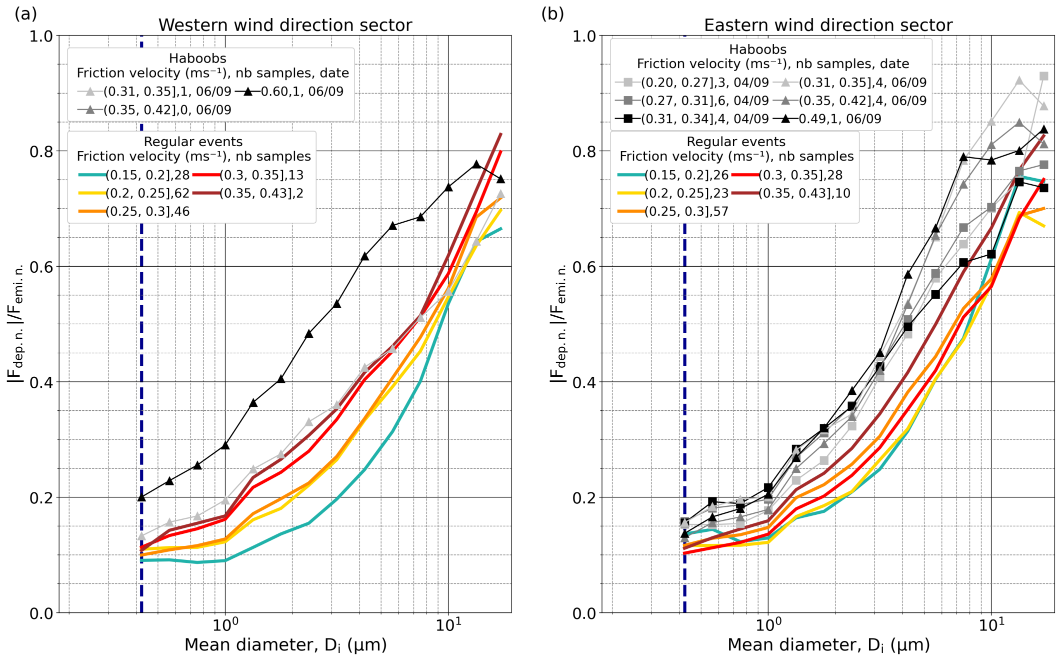

Figure S32. Ratio of dry deposition flux to the estimated emitted dust flux, determined using the v_{dep} tuned parameterization, for different u_* intervals, types of events (regular or haboob) and wind directions in the range 150–330 ° (a) and 330–150°(b)

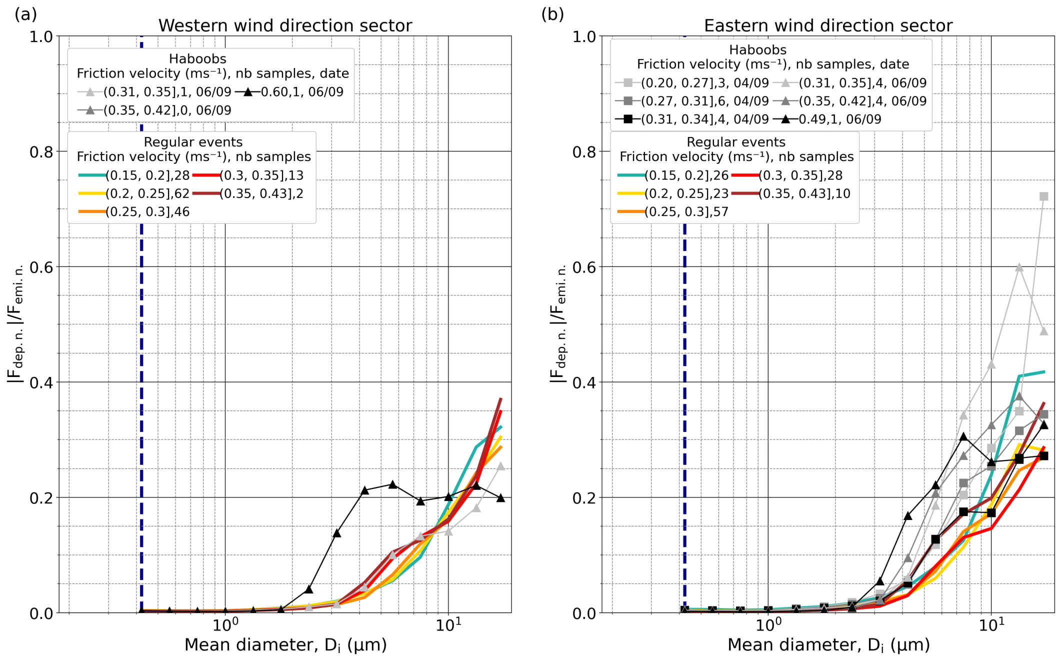

Figure S33. Ratio of dry deposition flux to the estimated emitted dust flux, determined using the v_{dep} F19, for different u_* intervals, types of events (regular or haboob) and wind directions in the range 150–330° (a) and 330–150° (b)

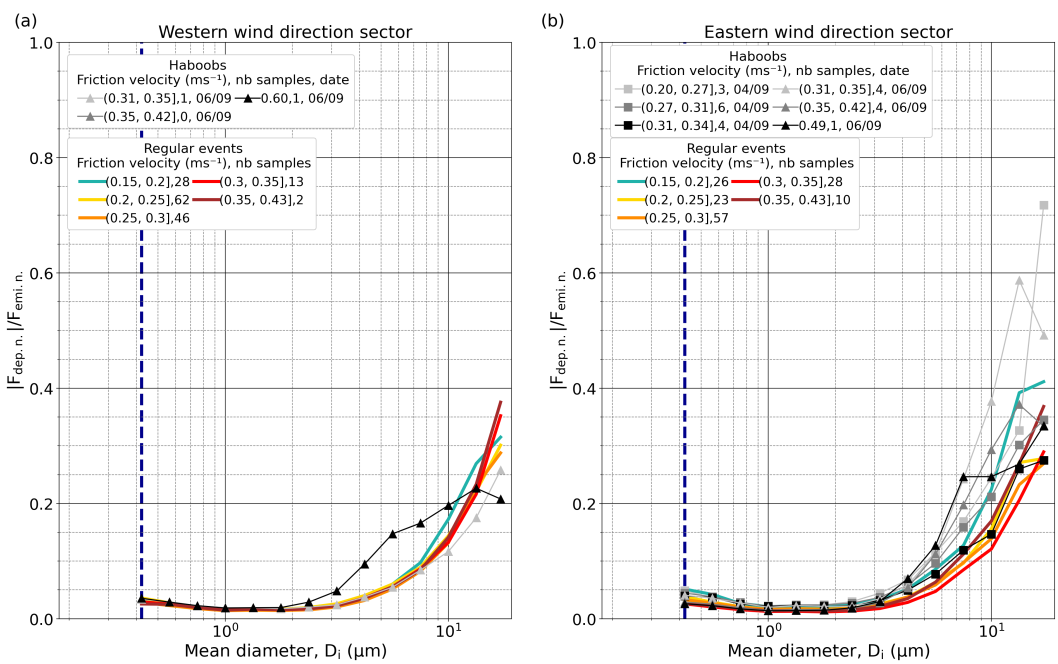

Figure S34. Ratio of dry deposition flux to the estimated emitted dust flux, determined using the v_{dep} Z01, for different u_* intervals, types of events (regular or haboob) and wind directions in the range 150–330° (a) and 330–150° (b)

References

Bergametti, G., Marticorena, B., Rajot, J.-L., Foret, G., Alfaro, S., and Laurent, B.: Size-resolved dry deposition velocities of dust particles: in situ measurements and parameterizations testing, Journal of Geophysical Research: Atmospheres, 123, 11–080, https://doi.org/10.1029/2018JD028964, 2018.

Chamberlain, A. C.: Roughness length of sea, sand, and snow, Bound. Lay. Meteorol., 25, 405–409, https://doi.org/10.1007/BF02041157, 1983.

Charnock, H.: Wind stress on a water surface, Q. J. Roy. Meteor. Soc., 81, 639–640, https://doi.org/10.1002/qj.49708135027, 1955.

Dupont, S., Rajot, J.-L., Labiadh, M., Bergametti, G., Alfaro, S., Bouet, C., Fernandes, R., Khalfallah, B., Lamaud, E., Marticorena, B., et al.: Aerodynamic parameters over an eroding bare surface: reconciliation of the law of the wall and eddy covariance determinations, J. Geophys. Res. Atmos., 123, 4490–4508, https://doi.org/10.1029/2017JD027984, 2018.

Fernandes, R., Dupont, S., and Lamaud, E.: Investigating the role of deposition on the size distribution of near-surface dust flux during erosion events, Aeolian Res., 37, 32–43, https://doi.org/10.1016/j.aeolia.2019.02.002, 2019.

González-Romero, A., González-Florez, C., Panta, A., Yus-Díez, J., Reche, C., Córdoba, P., Alastuey, A., Kandler, K., Klose, M., Baldo, C., et al.: Variability in grain size, mineralogy, and mode of occurrence of Fe in surface sediments of preferential dust-source inland drainage basins: The case of the Lower Drâa Valley, S Morocco, EGUsphere, 2023, 1–32, 2023.

Gorgas, J., Cardiel, N., and J., Z.: Estadística básica para estudiantes de ciencias, Departamento de Astrofísica y Ciencias de la Atmósfera, Universidad Complutense de Madrid, 2011.

Marticorena, B., Chatenet, B., Rajot, J.-L., Bergametti, G., Deroubaix, A., Vincent, J., Kouoi, A., Schmechtig, C., Coulibaly, M., Diallo, A., et al.: Mineral dust over west and central Sahel: Seasonal patterns of dry and wet deposition fluxes from a pluriannual sampling (2006–2012), Journal of Geophysical Research: Atmospheres, 122, 1338–1364, https://doi.org/10.1002/2016JD025995, 2017.

Martin, R. L. and Kok, J. F.: Wind-invariant saltation heights imply linear scaling of aeolian saltation flux with shear stress, Science advances, 3, e1602 569, https://doi.org/10.1126/sciadv.1602569, 2017.

Owen, R. P.: Saltation of uniform grains in air, J. Fluid Mech., 20, 225–242, https://doi.org/10.1017/S0022112064001173, 1964.

Sherman, D. J.: An equilibrium relationship for shear velocity and apparent roughness lenght in aeolian saltation, Geomorphology, 5, 419–431, https://doi.org/10.1016/0169-555X(92)90016-H, 1992.

Zhang, L., Gong, S., Padro, J., and Barrie, L.: A size-segregated particle dry deposition scheme for an atmospheric aerosol module, Atmospheric environment, 35, 549–560, 2001.